DROPLET IMPINGEMENT COOLING EXPERIMENTS ON NANO-STRUCTURED SURFACES

A Thesis

by

YEN-PO LIN

Submitted to the Office of Graduate Studies of
Texas A&M University
in partial fulfillment of the requirements for the degree of

MASTER OF SCIENCE

August 2010

Major Subject: Mechanical Engineering

Droplet Impingement Cooling Experiments on Nano-structured Surfaces

DROPLET IMPINGEMENT COOLING EXPERIMENTS ON NANO-STRUCTURED SURFACES

A Thesis

by

YEN-PO LIN

Submitted to the Office of Graduate Studies of
Texas A&M University
in partial fulfillment of the requirements for the degree of

MASTER OF SCIENCE

Approved by:

Co-Chairs of Committee,	Jorge L. Alvarado
	Debjyoti Banerjee
Committee Member,	Yassin A. Hassan
Head of Department,	Dennis O'Neal

August 2010

Major Subject: Mechanical Engineering

ABSTRACT

Droplet Impingement Cooling Experiments on Nano-structured Surfaces. (August 2010)

Yen-Po Lin, B.S., National Tsing Hua University, Taiwan

Co-Chairs of Advisory Committee: Dr. Jorge L. Alvarado
Dr. Debjyoti Banerjee

Spray cooling has proven to be efficient in managing thermal load in high power applications. Reliability of electronic products relies on the thermal management and understanding of heat transfer mechanisms including those related to spray cooling. However, to date, several of the key heat transfer mechanisms are still not well understood. An alternative approach for improving the heat transfer performance is to change the film dynamics through surface modification.

The main goal of this study is to understand the effects of nano-scale features on flat heater surfaces subjected to spray cooling and to determine the major factors in droplet impingement cooling to estimate their effects in the spray cooling system. Single droplet stream and simultaneous triple droplet stream with two different stream spacings (500 μm and 2000 μm), experiments have been performed to understand the droplet-surface interactions relevant to spray cooling systems.

Experiments have been conducted on nano-structured surfaces as well as on flat (smooth) surfaces. It is observed that nano-structured surfaces result in lower minimum wall temperatures, better heat transfer performance, and more uniform temperature

distribution. A new variable, effective thermal diameter (d_e), was defined based on the radial temperature profiles inside the impact zone to quantify the effects of the nano-structured surface in droplet cooling. Results indicate that larger effective cooling area can be achieved using nano-structured surface in the single droplet stream experiments. In triple stream experiments, nano-structured surface also showed an enhanced heat transfer.

In single stream experiments, larger outer ring structures (i.e. larger outer diameters) in the impact crater were observed on the nano-structured surfaces which can be used to explain enhanced heat transfer performance. Smaller stream spacing in triple stream experiments reveal that the outer ring structure is disrupted resulting in lower heat transfer. Lower static contact angle on the nano-structured surface has been observed, which implies that changes in surface properties result in enhanced film dynamics and better heat transfer behavior. The results and conclusions of this study should be useful for understanding the physics of spray cooling and in the design of better spray cooling systems.

DEDICATION

To God for his blessing.

To my family for their unconditional love.

To Dr. Jorge L. Alvarado for his inspiration and support.

ACKNOWLEDGEMENTS

First, I would like to express my heartfelt gratitude to Dr. Jorge L. Alvarado for identifying my research potential. I am grateful for his guidance and support throughout the course of my research at Texas A&M University. He is undoubtedly a great mentor for my academic and professional pursuits.

I would like to acknowledge Dr. Debjyoti Banerjee for being my co-chair and for sharing his expertise in the field of multi-phase heat transfer and nano-fabrication. I would like to thank Dr. Yassin A. Hassin for being my committee member and for his helpful advice on my research topic. I am grateful for the patient assistance and discussion provided by Guillermo Soriano in Spray Cooling Laboratory through the experiments. I also acknowledge the Office of Naval Research (ONR) for providing the funding for my research.

I would like to thank faculty, staff, and friends in the Microelectronics Research Center (The University of Texas at Austin) for guiding and assisting me through the nano-fabrication process as well as for their constant equipment support.

Thanks also go to my friends, faculty and staff of Texas A&M University for making my time at College Station a great experience. I also want to extend my gratitude to all the people who have helped me and all the researchers in the previous studies in this field for making my work possible.

Finally, I would like to thank Yen-Song and Yen-Ting for being the best siblings, and my parents for their encouragement, patience, support, and most important of all, their never-ending love.

TABLE OF CONTENTS

Page

Page

Page

LIST OF FIGURES

Page

Page

Page

Page

Page

Page

LIST OF TABLES

Page

Page

1. INTRODUCTION AND LITERATURE REVIEW

Temperature control in high power applications is getting more and more critical in the present day. These applications include cooling of electronics components, laser, aircraft, and nuclear power plant to name a few. Heat accumulation in devices usually results in undesirable high working temperature which causes serious safety problem and decrease reliability and product lifetime. Innovative heat removal techniques are required to solve this urgent situation to improve the efficiency and reliability of electronic systems in particular. In the published literature, high-flux and ultra-high heat flux ranges have been identified [1]. In those particular cases, phase change cooling methods are the only ones that can be employed including pool boiling, jet impingement cooling, and spray cooling. Among all the phase change cooling approaches, spray cooling is thought to be the most appropriate for future ultra-high-heat flux applications due to its heat transfer capability and uniformity. In a previous study, over 1200 W/cm^2 at low wall superheat had been achieved using water as working fluid [2].

The advantage of using spray cooling is that the surface temperature distribution is more uniform in comparison to the jet-impingement cooling. Compare to pool boiling, critical heat flux (CHF) for spray cooling is much higher because of the strong forced convection taking place on the surface.

This thesis follows the style of International Journal of Heat and Mass Transfer.

1.1. Spray cooling

In a typical spray cooling setup, atomized liquid sprays are generated which impact onto a heated surface. Spray nozzles can be identified into two categories: (a) pressure-atomized and (b) air-atomized nozzle. The pressure-atomized nozzles use high-pressure liquids to form the spray. On the other hand, air-atomized nozzles rely on high pressure air to assist liquid breakup and spray formation. Heat is then dissipated by the atomized droplets through sensible heating, latent heating, and forced convection. This method has been proven to be very effective and promising.

There are four main mechanisms in the spray cooling system including: 1) intense convection, 2) secondary nucleation, 3) thin-film evaporation and 4) nucleation at the heater surface (Fig. 1). Intense convection is caused by impinging droplets where heat is dissipated by forced radial convection while the fluid remains in the liquid phase. Secondary nucleation is caused by air bubbles which are brought by impingement liquid to film generating nucleation sites for heterogeneous nucleation. Thin film evaporation is caused by the liquid molecular escaping from the film into the environment. Nucleation at the heater surface is in the form of vapor bubbles of the liquid formed at the surface (i.e. pool boiling).

However, heat dissipating capability in spray cooling is determined by numerous correlated factors including coolant type, nozzle type, nozzle-to-surface distance, droplet diameter, droplet frequency, droplet velocity, surface conditions and volumetric flow rate. The study of each parameter independently in a spray cooling set-up is difficult and

very time-consuming. This leads to a lack of understanding which limits predictability of the heat dissipation capabilities of a spray cooling systems.

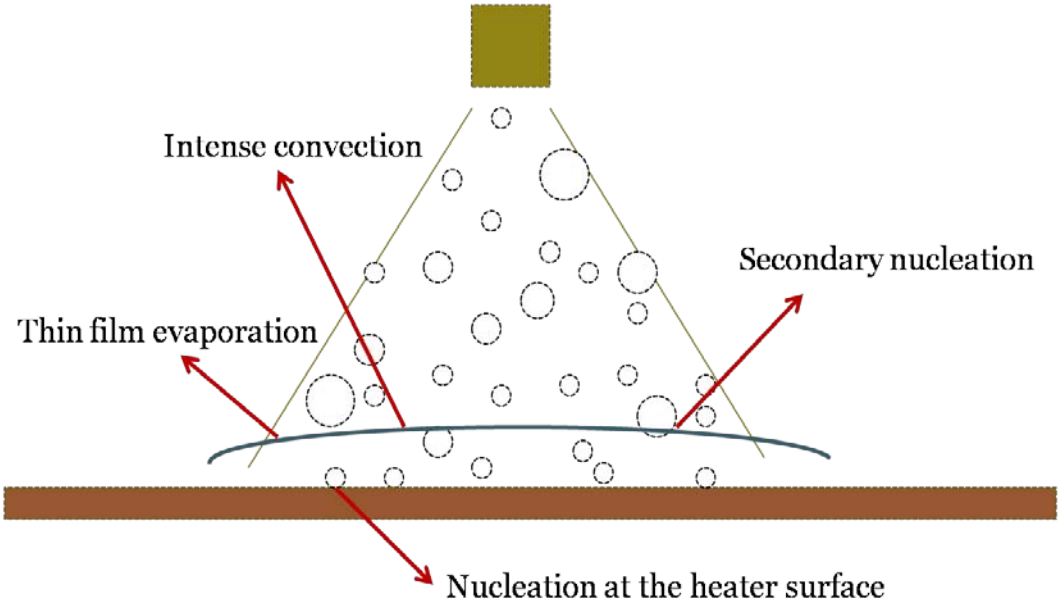

Fig. 1. Four main mechanisms in a spray cooling system

1.2. Literature review

1.2.1. Parametric study

For the last decades, numerous studies have been carried out in order to characterize the dominating parameters responsible for high heat transfer in the spray cooling. In early studies, Toda [3] observed that the heat transfer curve of the spray cooling has similar characteristics to the typical pool boiling curve. In that work, he also showed that spray volumetric flux has the strongest effect on cooling performance while the sub-cooling of the spray liquid had a minor effect.

In the work of Monde [4] and Mudawar et al. [1, 5, 6], several parameters of spray cooling were studied and concluded that CHF is the mostly dependent on the volumetric flow rate. Mudawar [5] also suggested that Sauter mean diameter and nozzle-to-surface distance have strong influence on spray cooling. Horacek et al. [7, 8] used a transparent heater array consisting of 96 micro heaters where each heating element could be individually controlled to study the key mechanisms of spray cooling. They used the total internal reflectance (TIR) technique to visualize and measure contact line length (CLL). The three phase contact line is where the solid, liquid and vapor phase meet. They suggested that heat flux is directly related to CLL. Their results showed that CLL increased with superheat (T_s-T_{sat}), reaching maximum at CHF, and then decreased as the surface began to dry out.

1.2.2. Surface enhancement study

Pais et al. [2] studied the effects of surface roughness on spray cooling. Their results revealed that the onset of nucleate boiling occurs at low superheat values. The authors attributed the heat transfer enhancement to early bubble departure from the surface during nucleate boiling. They also concluded that secondary nucleation becomes the primary role in heat transfer mechanism in smooth surfaces.

Sehmbey et al. [9] further studied the effect of surface properties on spray cooling. Different kind of surfaces material including two grit-polished copper surfaces were tested using deionized water and air-atomized nozzles. Higher heat transfer performance but no significant influence on the CHF were observed on the surface with larger contact

angle (gas phase to liquid phase). They also found that higher surface roughness decreases the cooling performance of the spray due to an increased film thickness. However, enhancement in CHF is only reached within certain roughness range. Further surface modification showed no further enhancement in heat transfer.

Silk et al. [10] studied the effects of surface enhancement in spray cooling using cubic fins, pyramids and straight fins in the millimeter scale. They found that the heat transfer performance was improved for all surfaces when compared to a flat surface while inclination angles of the spray have little effect. They attributed this enhancement to the increase of the effective heat transfer area and CLL. They also investigated the influence of dissolved gas and found the improvement was more significant for degassed fluid.

Hsieh and Yao [11] studied the influence of surface micro-structures on spray cooling using a pressure atomizer nozzle. They attributed heat transfer enhancement to changes in capillary forces in the film due to the surface structure. Smaller surface structures resulted in better heat transfer performance. Bond number of the microstructures was concluded to be the primary factor responsible for the heat transfer enhancement on the micro-structured surfaces.

Sodtke and Stephan [12] also examined the effect of microstructure and showed that spray cooling on micro-structured can lead to significantly improved in cooling performance compared to smooth surfaces at the same superheat. The authors believed this effect was due to an increase of the CLL which takes place when the liquid film

thickness decreases during heat transfer exposing the protruded microstructures as discussed and explained by Horacek et al. [8]. An infrared camera was used to show that for a smooth surface the dissipated heat flux increases with an increase in CLL. Experimental results on three different kinds of the micro-pyramid structured surfaces were used to explain these results. They suggested that the effect of using microstructure is only significant in the thin film evaporative region and partial dry out region. In these two regions the micro-structures start protruding when the coolant thickness decreases resulting in larger CLL.

J. H. Kim et al. [13] and Y. Kim et al. [14] studied the effect of micro-porous media. They used water as coolant at room temperature and found that CHF increased for all examined micro-porous surfaces. Both studies reveal that cooling performance is most efficient in the evaporative zone. Surfaces coated with different particle sizes were also investigated and showed little effect on the cooling performance. In addition, Y. Kim et al. [14] claimed that liquid flow rate has no effect on the CHF.

1.3. Motivation and objective

Given the state of knowledge, it became evident that the use of nano-structured surfaces in spray cooling should be studied in more detail. The interaction between impinging droplets and nano-structured surfaces needs to be studied to be able to understand the role of film dynamics on heat transfer.

In pool boiling studies, Sriraman and Banerjee [15] examined the effect of nano features on surfaces using PF-5060 as coolant. In their study, a nano-fin array was

fabricated using nano imprinting technology. The results showed that under saturation condition, the CHF for nano-structured surface increases by 41% in comparison to a bare surface. The authors concluded that an observed lower contact angle on the nano-pin finned surfaces could be one potential explanation for the improvement of CHF. Bubble nucleation, growth and departure process also increased.

The objective of this study is to determine the effect of nano-structured surfaces on droplet impingement cooling. This is the first study known to date that will illustrate the interaction between nano-scale features and single and multiple droplet impingement heat transfer. Single and triple droplet stream impingement cooling experiments have been performed in an effort to minimize the number of physical parameters necessary to elucidate the main mechanisms in spray cooling system.

In this study, a specific design of surface structure used in Sriraman and Banerjee's study [15] was adopted and fabricated using step and flash imprinting lithography (S-FIL) followed by several steps of thin film heater deposition. The purpose of this work is to obtain thin test samples around 300 μm in thickness which allows temperature distribution to be recorded from the backside of samples. The technique allows for real temporal and spatial response of surface temperature of the heater surface where the droplet cooling occurs. Single and triple stream experiments were carried out using different orifice plates attached to the droplet generator. The fabrication processes, experimental set-up and test procedure are summarized in below.

2. FABRICATION OF TEST SURFACES

2.1. Nano-structure fabrication

The aim of this work is to study the effect of the nano features on the droplet impingement heat transfer. The nano fabrication technique used in this study is the step and flash imprint lithography which has been widely used in the nano fabrication industry. The introduction, theory and fabrication process of step and flash imprint lithography used in this study is summarized in the following sections.

2.1.1. Step and flash imprint lithography

Step and Flash Imprinting Lithography (S-FIL) is a nano fabrication technique developed by C.G. Willson and S. V. Sreenivasan's research group [16, 17] at the University of Texas at Austin. S-FIL defines and reproduces surface features based on a low viscosity Ultra Violet (UV) curable fluid that fills the cavities of a transparent quartz template. The pattern on the template is defined by electronic-beam lithography. After UV cure, the surface features are formed onto the substrate and are transferred onto the under-layer by successive etching steps.

There are several advantages of using the S-FIL. Compare to other lithography methods used in the traditional semiconductor industry, it is relatively cheap because defining surface features through the physical contact in the S-FIL requires simpler and cheaper mechanical components instead of expensive high accurate optical lenses used in the traditional lithography methods. In addition, the feature resolution of the S-FIL is

determined by the template only instead of light source wavelength as it is the case in optical lithography. Therefore there is no scattering effect in S-FIL. Patterned features on the template are fabricated using electronic beam lithography, which makes it easy to fabricate sub-30 nm surface features. Once the template is fabricated, S-FIL is considerably faster in comparison to electronic-beam lithography for large area fabrication. The typical photopolymerization time takes just few seconds and thereafter enables S-FIL to repeat the imprinting process on the substrate within a small time.

Furthermore, compare to other nano-imprinting lithography (NIL) methods, S-FIL is accomplished under room temperature and uses only small pressing pressure which avoids thermal deformation and increases accuracy. The difference between S-FIL and other NIL is that the transparent template used as mold and the UV curable liquid are used in S-FIL to define the objective pattern. Low viscous UV-curable chemical liquid first fills the template cavity by pressing template onto the surface which is photopolymerized by UV-light to obtain the desired pattern. Each template consists of a patterned effective area of 10 mm by 10 mm or 25 mm by 25 mm which is called mesa. Combined with step imprint process, mesa is used to define the pattern onto the substrate up to 8-inch wafer by repeating these steps, which significantly reduces production time.

S-FIL processe was used in this study to fabricate nano pillar arrays as shown in Fig. 2. First, low viscous UV curable liquid was dispensed on the surface. Second, the template was pressed onto the surface to force the dispensed liquid fill the cavity on the template which was then photopolymerized by UV light source. After releasing the

template, several etching processes were undertaken using reactive iron etch (RIE) to transfer the pattern onto the substrate. Details are described in the following sections.

2.1.2. Fabrication procedure

2.1.2.1. Template preparation

Template pattern

The template consists of a square array of nano holes, which are 100 nm deep with an average diameter of 200 nm, and a lateral pitch of 1 μm from center to center. Template pattern was fabricated using electronic beam lithography. After imprinting, the pattern leaves 200 nm diameter pillars with a height of 100 nm. Prior to imprinting, the template was prepared and carefully examined to ensure the quality of the fabrication process. All the key steps are explained in detail below.

Template clean

A clean template is essential to ensure imprinting quality. Every time prior to imprinting, a piranha solution was used to remove remaining organic matter and small particles left on the template surface using the acid hood.

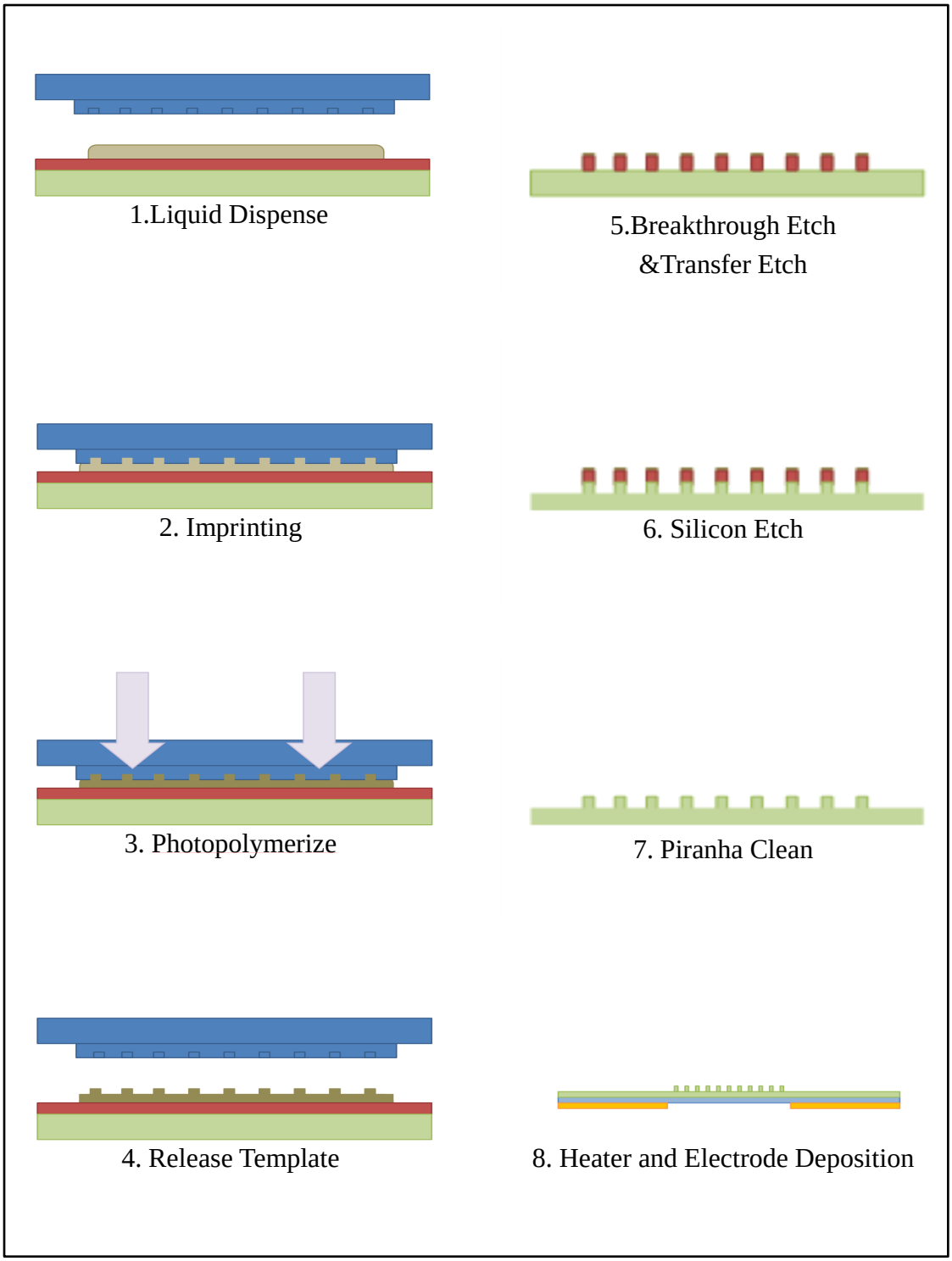

Fig. 2. Nano fabrication process of test surfaces

Piranha solution is a strong oxidizer which removes organic residues from the substrates effectively. It was prepared by 1 part of hydrogen peroxide and 2 parts of sulfuric acid. In this experiment, 825 ml of hydrogen peroxide and 1650 ml of sulfuric acid were prepared and mixed by slowly adding sulfuric acid into hydrogen peroxide. Care was taken because it was an exothermic reaction. The process required 5 minutes for the solution to stabilize. During preparation, Piranha solution was heated to 100-110 °C by the heating plate to enhance cleaning ability.

After the Piranha solution was prepared, the template was immersed in Piranha solution for 15 minutes and then rinsed by DI water in the cascade rinser for 5 rinse cycles. Before DI water was rinsed, template had to be cooled down for at least 5 minutes to prevent breakage by thermal shock. Another piranha preparation and cleaning cycle was done with the exception that the template was rinsed by DI water for 10 times. After cleaning, the template was dried using nitrogen gas. In this process, iso-propyl alcohol (IPA) was first poured on the template to shorten the drying time.

Silane surface treatment

After cleaning, template was left in a silane surface treatment protocol with mesa facing up for 10 hours before getting ready to imprint. Silane treatment was prepared by 0.2% wt Dimethylchloro-silane solution in Toluene. In this procedure, a thin coating was formed on the template which prevented the etch barrier (low viscous UV curable liquid) from sticking on the template and helped dispense barrier uniformly by spreading out the mesa during the imprinting process.

2.1.2.2. Substrate preparation

Wafer clean

Double Side Polished (DSP) wafers were used in the S-FIL process because of better control of surface variation. In this study, 4-inch DSP silicon wafers were used. First, DSP silicon wafers were cleaned by placing them in Piranha solution for 8 to 10 minutes without heating. After Piranha cleaning, wafers were rinsed with DI water in the cascade rinser for 10 rinse cycles. Cleaned wafers were loaded onto a Verteq Spin/Rinse Dryer (Akrion, Inc.) and spun dry before spin-coating the transfer layer.

Spin-coating of the transfer layer

The transfer layer which has good adhesion properties and high etching selectivity relative to the substrate was spin-coated onto the substrate prior to imprinting. Less than 1 ml of the transfer layer was filtered and dispensed on the silicon substrate. After spin-coating, the wafer was baked at 180 °C for 1 minute. A transfer layer coating of approximately 60 nm in thickness was obtained.

During imprinting, the transfer layer assisted in filling the template cavity through capillary action. After UV curing, the transfer layer promoted adhesion of the imprint resist to the substrate. Purpose of using the transfer layer was to obtain high aspect ratio structures by taking advantage of its high selectivity property. During the RIE process, a transfer layer acted like a mask which protected the material located underneath from being etched out.

2.1.2.3. Imprinting process

The IMPRIO 100 by Molecular Imprints Inc. was used in Microelectronics Research Center at the University of Texas at Austin. The imprinting process was controlled and monitored by the user through a Graphic User Interface (Molecular Imprints, Inc.). Prior to imprinting, the prepared template and wafer were loaded and aligned to ensure proper inclination and alignment. These semi-manual processes were essential to ensure the imprinting quality.

Load the template

The alignment of the template was done by focusing the horizontal edge of the mesa. There are two alignment screws necessary to adjust the template to the required accuracy. Then the template was loaded in the vacuum chuck. Template leveling was done afterwards to ensure the mesa was held exactly parallel to the substrate below. The leveling was performed in order to get more uniform imprints. A 4-point strategy was initially chosen to measure the level and angle of inclination. After each measurement, manual adjustments were performed using the adjustment screws. Several measurement steps were followed until the desired accuracy was achieved. Higher accuracy can be achieved by using the 12-point measurement strategy.

Load the substrate

After alignment of the template, the substrate was loaded using the automatic substrate loading system in the IMPRIO 100. The alignment and leveling of the substrate

was performed automatically relative to the positioned template. Therefore, the substrate had to be realigned if the template was changed.

Imprinting the pattern

The imprinting process has a certain degree of flexibility by allowing the distance between each imprint (the "street size") to be adjustable using the software interface. The software allows a user to make the most use of the substrate to fit the application. In this study, the street size of 0.5 mm street size was used in order to fit the desired heater design.

Dispense etch barrier layer and droplet pattern

UV curable fluid with low viscosity was dispensed onto the area that would be imprinted and exposed. In this step, care was taken to ensure no bubbles were trapped which could cause structural defects.

Imprinting quality is highly influenced by dispense liquid pattern. Trapped bubble during imprinting and fringing alone the imprint edge could result in incomplete imprinting. Therefore, care was taken to ensure air bubbles did not get trapped, and fringe edge was not generated during the process. Droplet pattern was modified by user using the software. Number of droplets, location of each droplet, and total volume was determined using the control panel interface. It required several attempts before getting good imprinting result. A good imprinting should have uniform feature as well as smooth edge along the mesa boundary. A low 0.035 µl droplet volume was used in this study.

Imprinting and exposure

Template was then push down to the surface, while a low viscosity etch barrier filled the template cavity under low pressure. Before releasing the template, UV light was used to cure the dispensed fluid. The template was then released from the surface after UV curing process. A good imprint would have exhibited appropriate release force. A successful imprint is thin and uniform. In addition, a light blue and uniform color should be observed after good imprinting.

The UV curing step was defined in the system by the user with the pre-exposure time, exposure time and the post exposure time. Pre-exposure time was specified to allow the resist to fill all the recesses in the template, which depended on the intricacy of the pattern on the template. For the present study, a pre-exposure time of 110 seconds was used. Typically, exposure time was about 10 seconds with no post-exposure.

Etching

After imprinting, several dry etching steps were undertaken to transfer the imprint pattern onto the substrate. Plasmatherm 790 RIE system was used in this stage to perform the reactive ion etch (RIE). There are three steps involved including (Fig. 3):

(1) Breakthrough etch

Anisotropic etch that removes the residual layer to break through the underlying transfer layer. The residual layer is the remaining layer during imprinting that should be

removed prior to the next transfer of the pattern. The breakthrough etch was done using CHF_3 and O_2 gas-based etchers.

(2) Transfer layer etch

In this process, the patterned imprint resist features were used as an etch mask to protect the underlying transfer layer. The transfer etch was done by using an O_2 gas-based etcher. The transfer layer not covered by the etch barrier was then etched out to reveal the underneath silicon substrate.

(3) Silicon etch

After the transfer etch, RIE was again performed in the silicon etch step in order to obtain the silicon structure on the substrate. The silicon etch was done by using Cl_2 and HBr gas-based etchers. In addition, due to the high selectivity of the transfer layer, high aspect ratio structure could be obtained using deep reactive ion etch (DRIE).

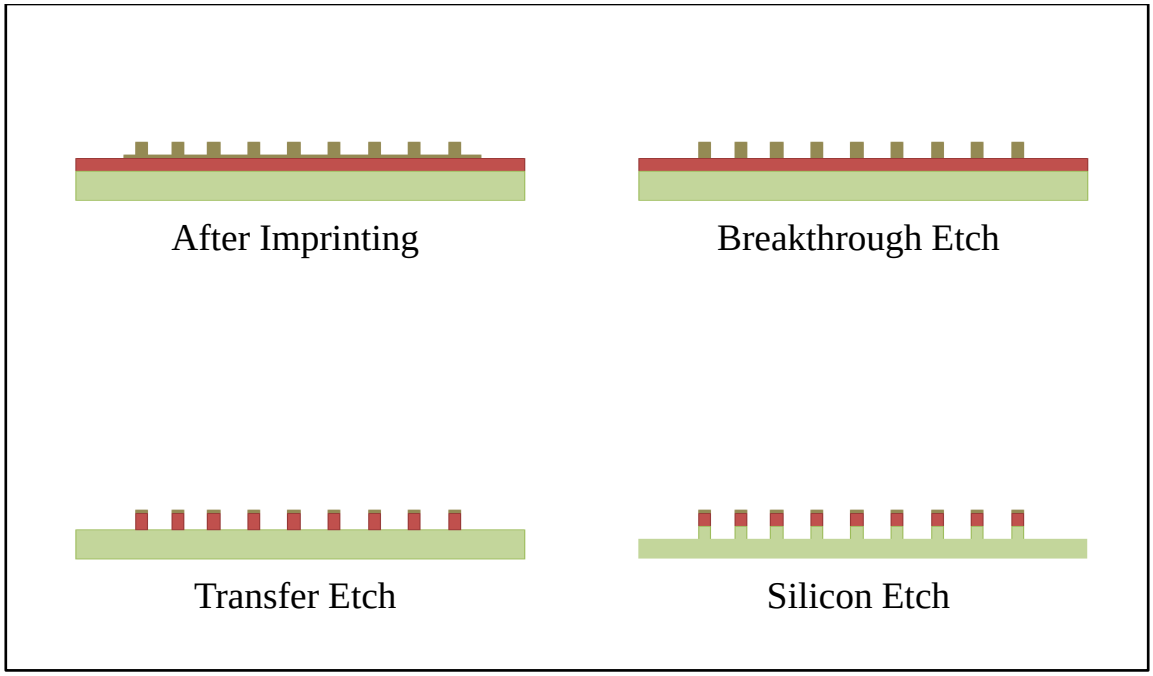

Fig. 3. 3-step RIE process after imprint

Removal of the remaining transfer layer and residual layer

After RIE, a Piranha oxidizer solution was used to remove the remaining transfer layer and residual layer from the surface. This final step of fabricating surface nano-structure is shown as step 7 in Fig. 2.

2.1.3. Test surfaces

After fabrication, the wafer was cut into 1.2 cm by 2.4 cm pieces yielding a 1.0 cm^2 nano-structured area in the center using a dicing tool. The heater design is shown in Fig. 4. These nano-structured areas consist of nano pillar arrays of 100 nm in height, 200 nm in diameter with 1.0 μm lateral pitch from center to center. Fig. 5 and Fig. 6 show the scanning electron microscope (SEM) and atomic force microscope (AFM) images of the

test surface. The nano pillar height was measured by AFM and shown to be around 100 nm.

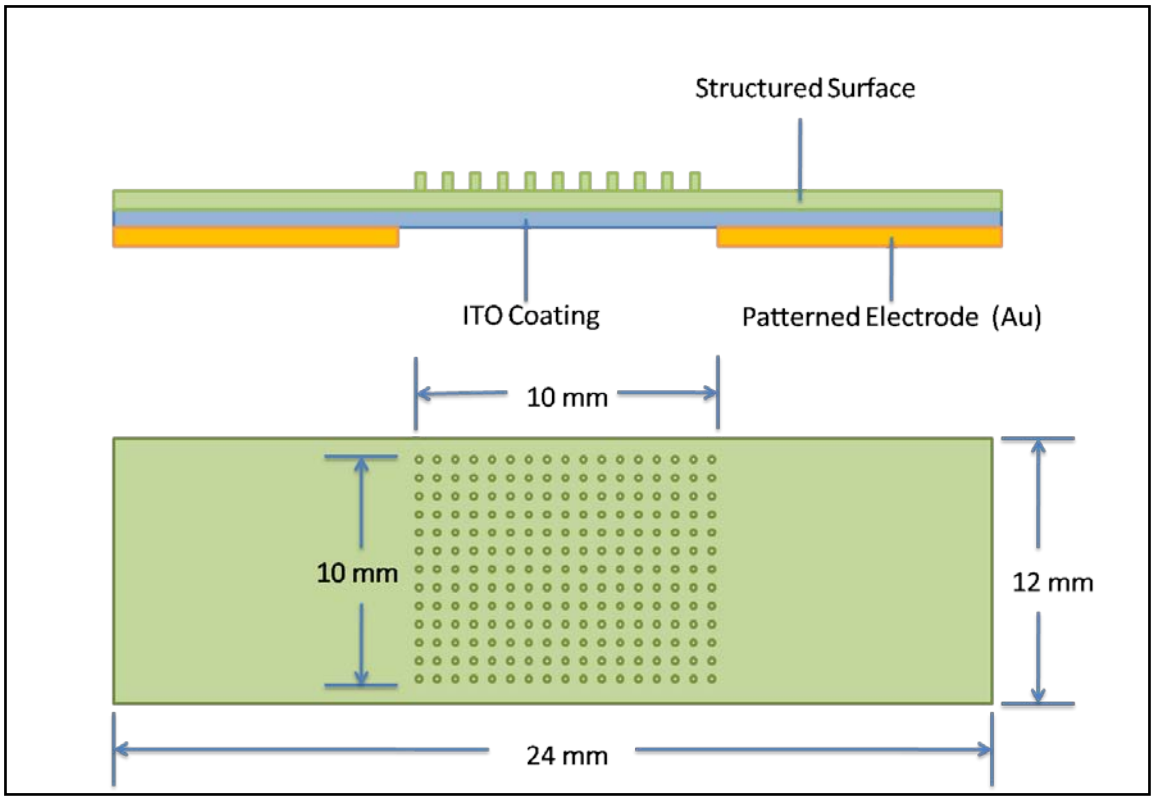

Fig. 4. Schematic diagram of the heater design (not to scale)

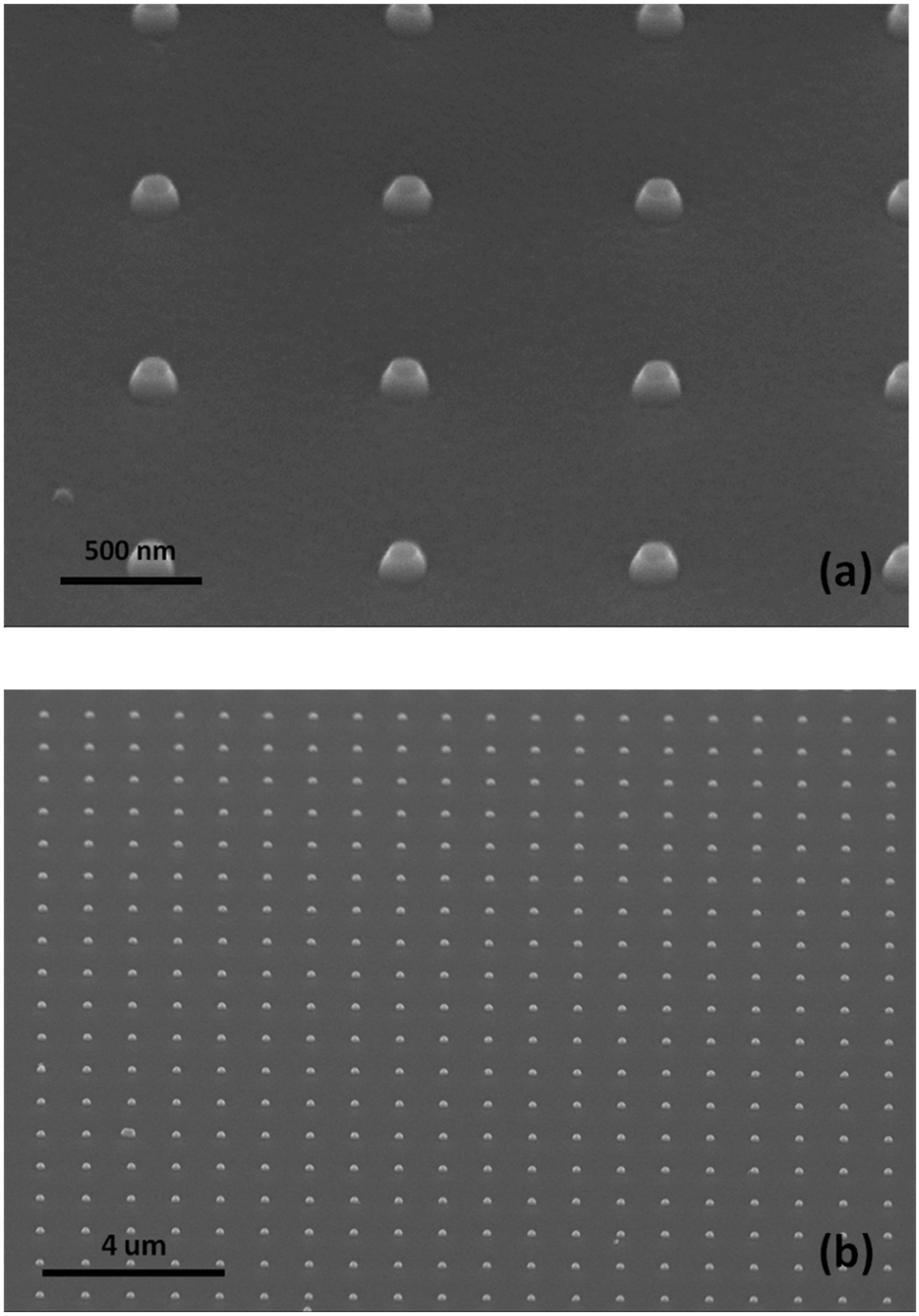

Fig. 5. SEM images of surface nano structure (a) closer view, (b) farther view

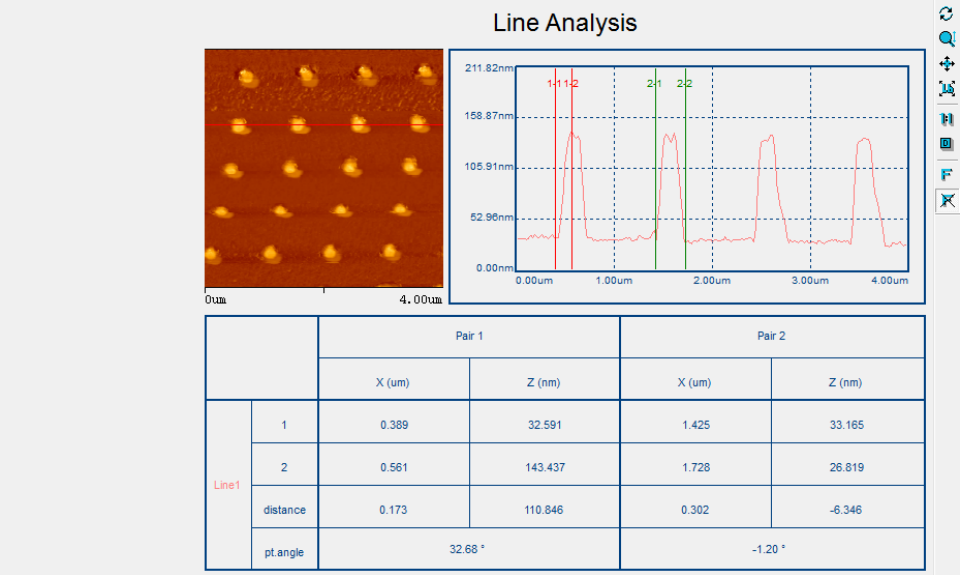

		Pair 1		Pair 2	
		X (um)	Z (nm)	X (um)	Z (nm)
Line1	1	0.389	32.591	1.425	33.165
	2	0.561	143.437	1.728	26.819
	distance	0.173	110.846	0.302	-6.346
	pt.angle	32.68 °		-1.20 °	

Fig. 6. Atomic force microscope (AFM) scanning image of surface nano structure

2.2. Heater and electrode deposition

Heater and electrode were made by depositing several materials on the bottom of the silicon wafer. A 50 nm thick nickel and a 300 nm thick indium tin oxide (ITO) were deposited using the sputter deposition technique first to act as thin film heater in the study. The nickel layer was used as adhesive layer to help stick the ITO to the surface. After heater deposition, a thin layer of gold with a thickness of 100 nm was deposited on both ends of the heater as shown in Fig. 7. Constant heat flux conditions were imposed on the ITO coating by taking advantage of Joule heating effect by using direct current through two patterned electrodes. Since the heater was chemically (solid state) bonded to the substrate, the thermal resistance between the heater and heating surface was considered to be minimal

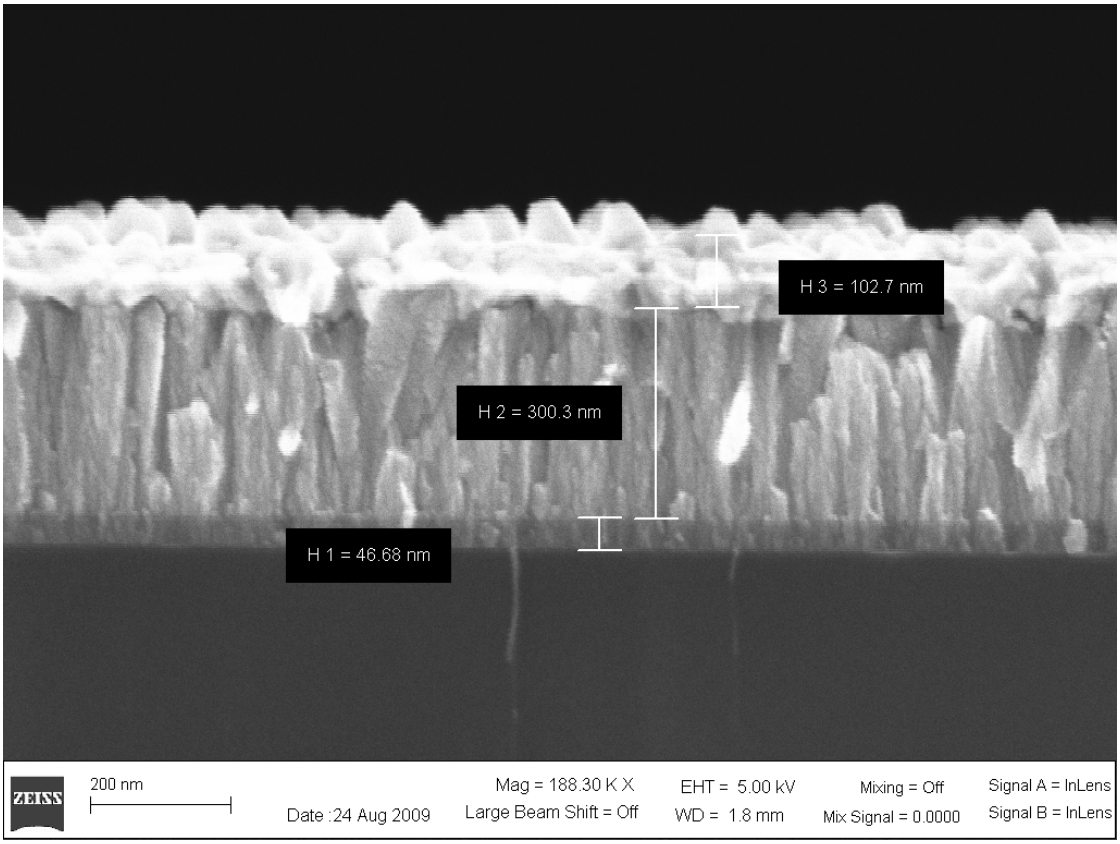

Fig. 7. SEM image of patterned adhesive nickel layer (H 1), ITO thin film heater (H 2), and gold electrode (H 3)

3. EXPERIMENTAL SETUP AND PROCEDURE

3.1. System overview

The droplet impingement cooling experiment system consists primarily of the following three sub-systems:

1. Fluid supply and droplet generation system which generates and delivers the droplet onto test surfaces under controlled conditions.

2. Heater system that provides and maintains constant heat flux conditions on the test surfaces.

3. Data acquisition system for recording the high speed and IR images as well as processing experimental data.

Fig. 8 shows the schematic diagram of the droplet cooling (open) experimental set up with its different components. Each of the components is explained in detail below:

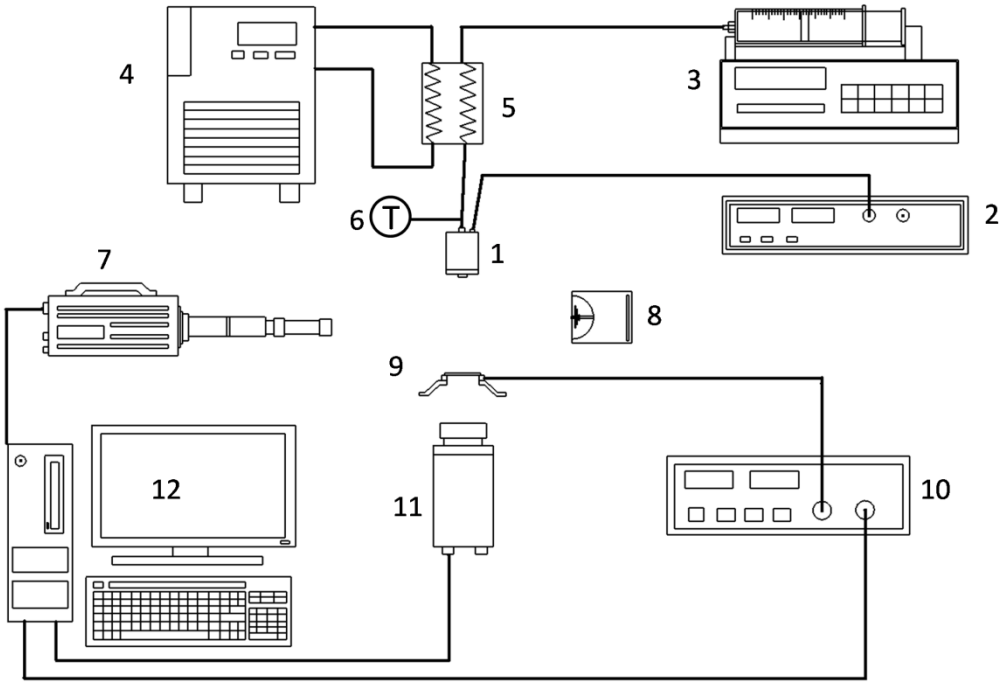

Fig. 8. Experimental apparatus: 1) droplet generator, 2) function generator, 3) syringe pump, 4) chiller, 5) heat exchanger, 6) temperature reading unit, 7) high speed camera, 8) backlight source, 9) heater assembly, 10) power supply, 11) infrared camera, 12) computer

3.1.1. Fluid supply and droplet generation system

The fluid supply and droplet generation system consists of a syringe pump, a function generator, a piezoelectric droplet generator, a heat exchanger, a temperature reading unit, and a heat exchange system. The working fluid was delivered to the heater surface as mono-dispersed droplets using a piezoelectric droplet generator. The frequency was controlled by a function generator (4011A, BK PRECISION) using a square wave during all the experiments. Droplets break as a result of the Rayleigh break-up mechanism. Two different orifice plates consisting of one and three 150 μm orifices

were used in this study to carry out single and triple stream experiments. Fluid supply flow rate was controlled by a syringe pump.

A chiller (MERLIN series m25, ThermoNESLAB) and a heat exchanger were used to control the fluid temperature. The fluid temperature was measured using a T-type thermocouple located at the inlet of the piezoelectric droplet generator. The droplet temperature was assumed to be at the measured temperature. Dielectric fluid FC-72 (Fluorinert, 3M Co.) was used as the working fluid in this study. The fluid properties at 1 atmosphere are shown in Table 1.

3.1.1.1. Single and triple droplet stream generation system

Two droplet impingement strategies were studied to understand droplet cooling heat transfer behavior of the single droplet. Furthermore, multiple impingement streams were also considered to elicit the interactions between neighboring impinging droplets. The two impingement strategies with their corresponding set ups are described in below.

Table 1
Fluid properties for FC-72 at 25 °C, 1 atmosphere

Saturation Pressure	P_{sat}	1 atm (101.325 kPa)
Liquid Density	ρ	1680 kg/m^3
Saturation Temperature	T_{sat}	56 °C
Latent Heat of Vaporization	h_{fg}	88 J/g
Liquid Specific Heat	C	1100 J kg^{-1} C^{-1}
Liquid Specific Heat	k_l	0.057 W m^{-1} °C^{-1}
Surface Tension	σ	10 dynes/cm

Single droplet stream system

Single droplet impingement experiments were undertaken by using a single orifice plate (Fig. 9). Mono-dispersed droplets were generated by making use of the Rayleigh break-up mechanisms. Parameters such as volume flow rate, droplet diameter, droplet frequency, and droplet velocity were considered in the study. By controlling the fluid

flow rate and frequency, the theoretical diameter of each droplet could be estimated by using the following equation:

$$d_{\mathrm{d}} = \left(\frac{6\dot{V}}{\pi f}\right)^{1/3} \quad (1)$$

Where d_{d} = diameter of the droplet, $\dot{V}$ = fluid volumetric flow rate, f = input perturbation frequency. The velocity of the droplet was obtained from measuring the recorded high speed images. Fig. 10 shows a high speed image of the singel droplet stream using FC-72 at 4500 Hz, 150 ml/hr.

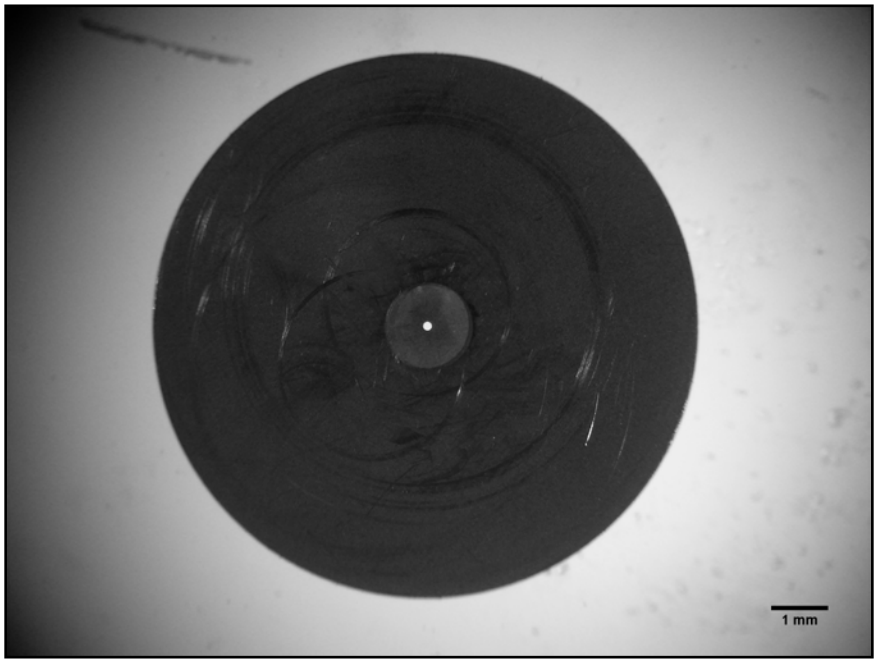

Fig. 9. Microscope image of the single orifice plate

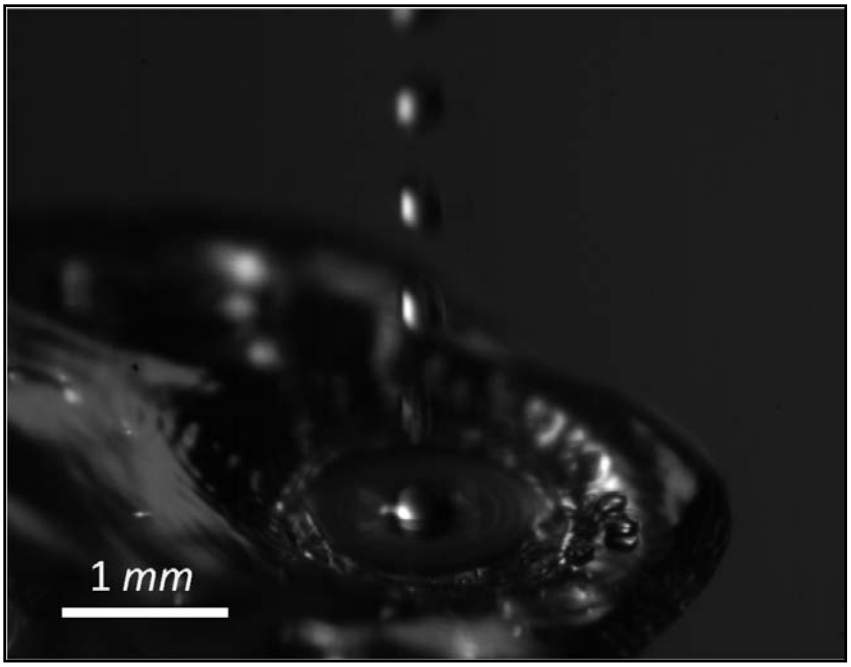

Fig. 10. High speed image of the single stream system using FC-72 at 20 °C, 4500 Hz, 150 ml/hr

Triple droplet stream system

Multiple (parallel) mono-dispersed droplet streams were obtained by using an orifice plate with three holes. The geometrical arrangement of the orifices on the plate determines the resulting droplet impingement array. In the present study, the orifice plate used in the multiple droplet experiments consisted of three 150 µm diameter orifices arranged in a single row with a 500 µm lateral pitch (spacing) between each other (Fig. 11). Each droplet had the same characteristics as the ones generated using a single-hole orifice plate when increasing flow rate from 150 ml/hr to 450 ml/hr. Fig. 12 shows a high speed image of the triple stream system at 4500 Hz with 500 µm spacing.

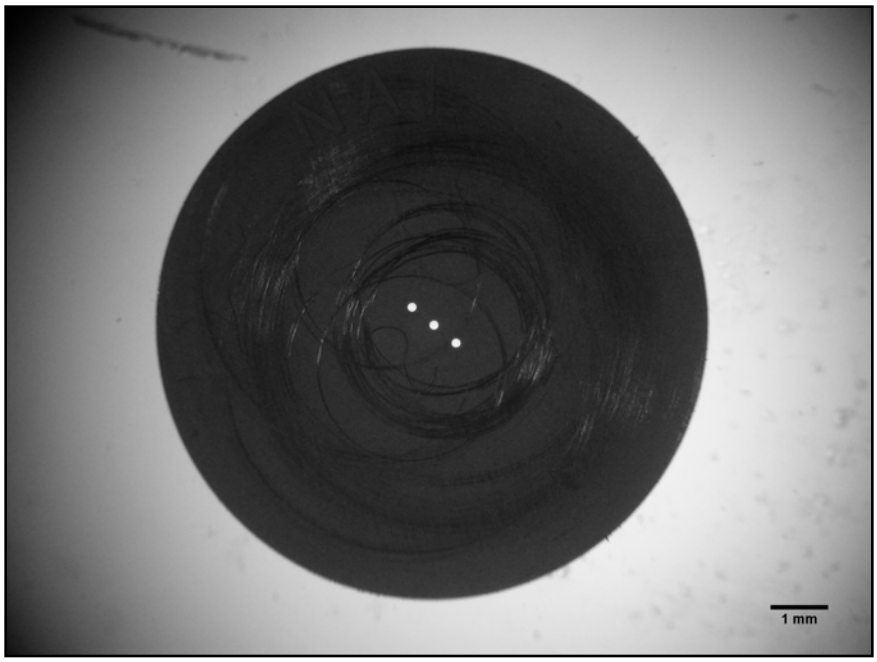

Fig. 11. Microscope image of the triple orifice plate

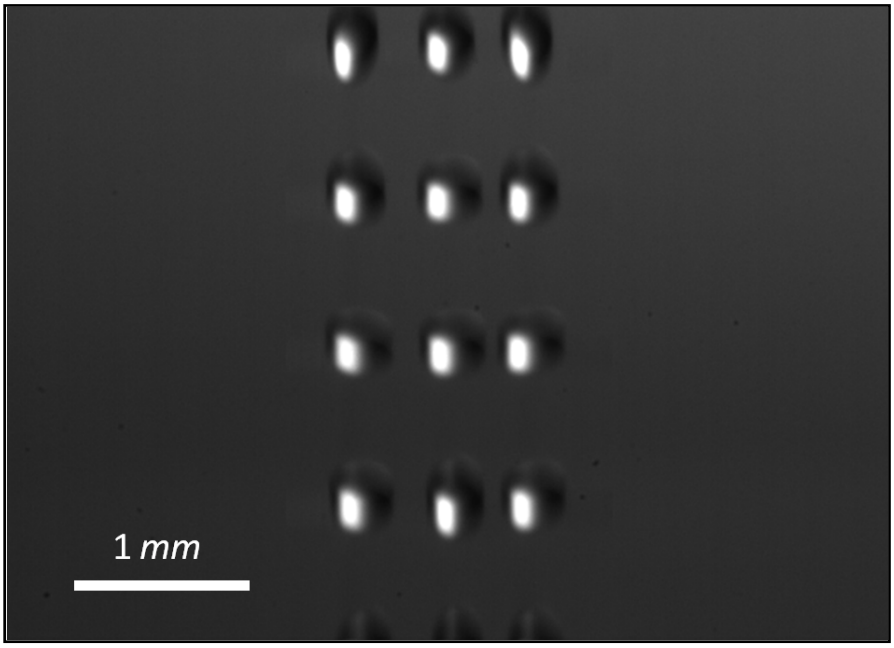

Fig. 12. High speed image of the triple stream system with smaller droplet stream spacing (500 µm) using FC-72 at 20 °C, 4500 Hz, 450 ml/hr

3.1.2. Heater system

The heater system includes the heater supporter and a power supply. Heaters were mounted on a Teflon holder using epoxy. Two copper wires were soldered on patterned electrodes using silver conductive epoxy to directly power the heater through a 1500 W power supply (Gensys600-2.6, LAMBDA). The power was connected to a computer that is used to control the input voltage.

3.1.3. Data acquisition system

The data acquisition system consisted of a high speed camera, a backlight source, an infrared (IR) camera, and a computer to process the data. The high speed camera (SA3, Photron) was used to measure the droplet diameter and to record the liquid film motion during each test. While taking high speed images, backlight illumination is required. An IR camera (FLIR A325, FLIR systems) was used to record the temperature data from the heater with a resolution of 320 by 240 pixels at 60 Hz. With a close up lens (Model AT197215), the spatial resolution and field of view were 100 μm and 32 by 24 mm respectively. This IR camera system was used for mapping the two-dimensional temperature distribution on the ITO surface.

3.2. Experimental procedure

The experimental procedure includes of several steps described in detail as the following.

3.2.1. Surface clean and fluid preparation

After mounting the heater on the holder, the test surface was cleaned and rinsed with IPA to wash off any organic particles residue left on the surface. After cleaning with IPA, the test surface was dried using compressed air. Three times of the procedure were undertaken to unsure the surface quality.

Before pouring the liquid into the syringe, FC-72 was filtered using a 20 μm filter. This step was essential to prevent particles from entering the generator which could cause clogging of the orifice. The filtered FC-72 was then poured into a 60 ml syringe and mounted on the syringe pump. The working fluid was then transported to the droplet generator through a thin tube which flowed through the heat exchanger. Before each test, the chiller was adjusted to the set temperature and run for at least 10 minutes until the coolant temperature reached thermal equilibrium.

3.2.2. Data acquisition system setup

After mounting the heater assembly on the test chamber, the focus of the IR camera was adjusted to ensure the accuracy at the predetermined magnification scale. The focus of the image was conducted through precisely adjusting the height of the IR camera. The high speed camera focus was adjusted afterwards in order to get clear image and precise magnification. After adjusting the data acquisition system, the position of the droplet generator was adjusted to ensure the droplet impinged on the nano-structured area of the test surface. The power supply was then connected to the heater assembly

and turned on to standby. After setting up the equipment, the experiment was ready to operate.

3.2.3. Data acquisition

Before applying power, the droplet generation system was turned on to prevent heater from burning out. The function generator was tuned up to the desired frequency, which was 4500 Hz in the present study. Slightly adjustments of frequency were required in order to obtain well mono-dispersed droplets. The high speed camera was used to check that the droplet break up mechanisms was taken place during the process. Environment temperature and relative humidity conditions were measured and recorded in a datasheet before the each test.

After droplets started hitting the surface, the power was then applied to the heater by controlling the input of the voltage. The power supply was controlled through the PC using Microsoft Hyper Terminal software. By using the software, it allows user to precisely control the input voltage and record correspond input amps. The heater system was considered to reach steady state conditions once surface temperature remained stable for at least 10 seconds.

3.2.3.1. High speed image recording

A high speed system was used to measure droplet parameters and to record film motion during the experiments. When operating, the backlight illumination was turned on. The images were recorded using 1,000 frames per second (fps) at a resolution of 1,024 by 1,024 pixels. The image analysis tool used in this study is the Vision Assistant

from National Instruments. The software was used to measure the projected vertical surface area of each droplet in order to compute droplet diameter. Crown diameters of the impact zone were measured and processed using the same software.

3.2.3.2. Temperature monitoring

The temperature of the heater was recorded using an IR camera located below the heater set up. The IR camera was connected to a computer using an Ethernet and controlled using ExaminIR software (FLIR system). After the heater reached steady state conditions, IR images were recorded at a rate of 60 Hz. Recorded thermal images were exported as Comma Separated Values (CSV) file that is compatible for other software. Several MATLAB (MathWorks) codes were developed to process the data afterwards.

3.3. Heat flux calculation

Each heat flux value was calculated using the total power generated by the power supply divided by the effective area (Equation 2).

$$q'' = \frac{I \times V}{A} \quad (2)$$

Where I = the current value read on the Hyper Terminal, V = the voltage value read on the Hyper Terminal, and A = the effective area of the heater. It was assumed that heat loss of the soldered wire was negligible. The effective area was defined as the area of ITO film that was not covered by the gold electrodes.

3.4. Measurement uncertainty

The primary uncertainty of this experiment can be discussed in two different categories, which are uncertainty of heat transfer, and uncertainty of the image processing. One of the critical measurements of the experiments was minimum wall temperature for several heat flux values. Errors in heat transfer and temperature values come from two different sources including heat losses and IR image conversion to temperature data, respectively. Recent error analysis has shown that the heat flux uncertainty is about ±1.24 W/cm^2. A detailed analysis of heat flux uncertainty can be found in the appendix. The analysis of IR camera temperature reading indicates that there exist an uncertainty of ±0.8 ^oC at 40 ^oC and ±1.6 ^oC at 50 ^oC as explained in the appendix.

The other important uncertainties were generated by the image processing. In this research, the droplet diameter was measured under a magnification of 1.5 μm/pixel with a corresponding deviation of ±7.5μm. The crown diameter was measured by an average variation of ±4 pixels. Using a magnification of 5.88 μm/pixel, the crown diameter deviation was estimated to be ±24 μm or less than 1.7 %.

4. RESULTS AND DISCUSSION

4.1. Droplet characterization

First, the droplets parameters under test condition were characterized using the high speed imaging system and software. The measured parameters of the droplets for the single droplet stream impingement cooling experiments using FC-72 at 20 °C, 4500 Hz, 150 ml/hr are listed in Table 2. It is observed that the measured diameter of the droplet has a good agreement with the theoretical value which was obtained from equation (1).

Table 2
Measured droplet parameters under test condition

Volumetric Flow Rate (ml/hr)	Frequency (Hz)	Theoretical Diameter (µm)	Measured Diameter (µm)	Standard Deviation (µm)	Measured Droplet Velocity (m/s)	Standard Deviation (m/s)
150	4480	260	263.5	9.2	1.92	0.03

4.2. Single stream experiments

Single stream experiments were first undertaken to determine the effects of working fluid temperature and nano features on heat transfer. The results are discussed based on results of the thermal image, high speed image, minimum wall temperature, and radial temperature distribution inside the impact zone. Minimum wall temperature was used as a reference point to monitor the heat transfer effectiveness and was defined as the lowest temperature value inside the impact zone, which corresponds to the droplet impact point. Each of the recorded minimum wall temperature is an averaged value over 145 frames recorded by the infrared camera.

4.2.1. Real-time IR image comparison

The real time IR images of different surfaces are shown in Fig. 13-16. Each figure is an IR image snapshot. Fig. 13 and Fig. 14 show the bare silicon surface at low and high heat flux conditions, respectively. The droplet impact point can be identified from the IR image, showing that the surface temperature at the impact point is the lowest on the surface. The fluid boundary and bubble formation can be also observed on the bare silicon surface.

In Fig. 13, there are some bubbles generated near the impact point. Compare to the high speed image results taken from the heater top, these bubbles are generated outside the impact zone (distance are larger than outer ring diameter). The temperature at where bubbles appear is lower than in the surrounding fluid region on the surface, which is evidence that heat transfer is taken place inside the bubble. However, fluid boundary and bubble formation process are not observed as clearly on the nano-structured surface as on the bare silicon surface.

Fig. 15 and Fig. 16 show the results for nano-structured surface at low and high heat flux conditions, respectively. Fig. 15 and 16 show similar behaviors. Instead of fluid boundary and bubble formation process, larger areas with good temperature uniformity near the impact zone are observed on the nano-structured surface. This implies that the temperature distribution on the nano-structured surface is more uniform.

In order to quantify and illustrate different temperature distributions on the heater surface, time-averaged two-dimensional temperature profiles were used.

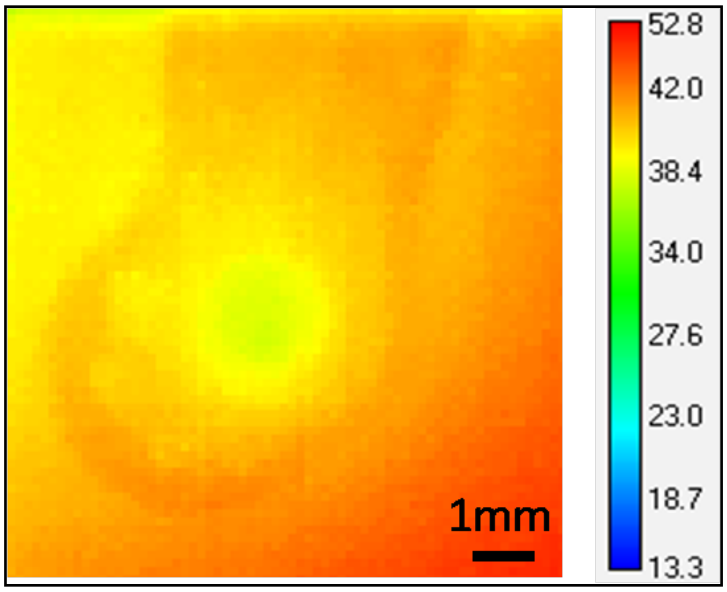

Fig. 13. Real-time IR image of bare silicon surface in the single droplet impingement cooling at low heat flux condition (10.1 W/cm^2)

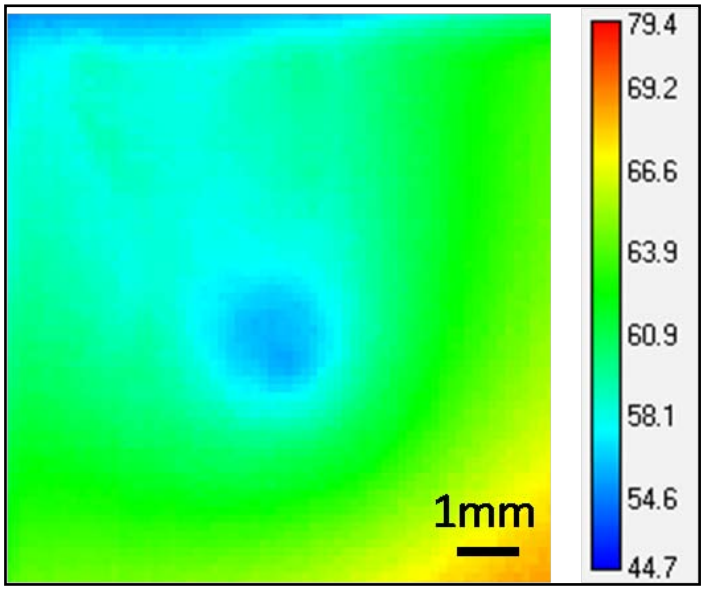

Fig. 14. Real-time IR image of bare silicon surface in the single droplet impingement cooling at high heat flux condition (19.6 W/cm^2)

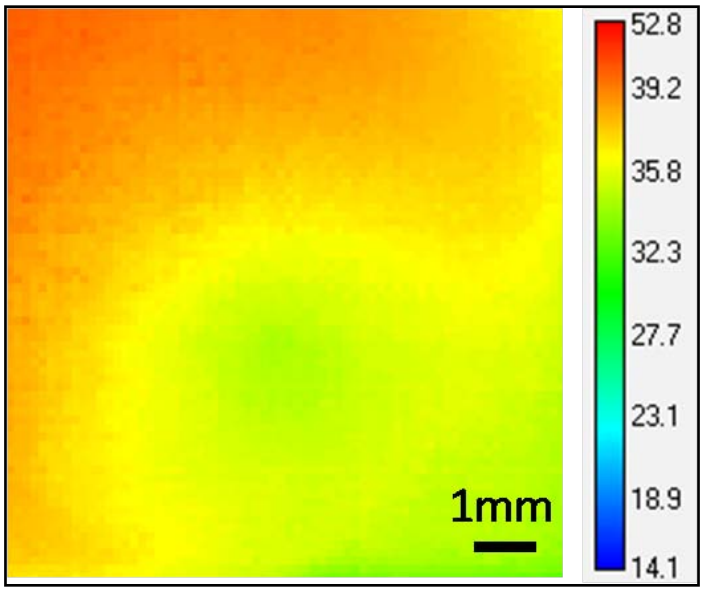

Fig. 15. Real-time IR image of nano-structured surface in the single droplet impingement cooling at low heat flux condition (12.8 W/cm^2)

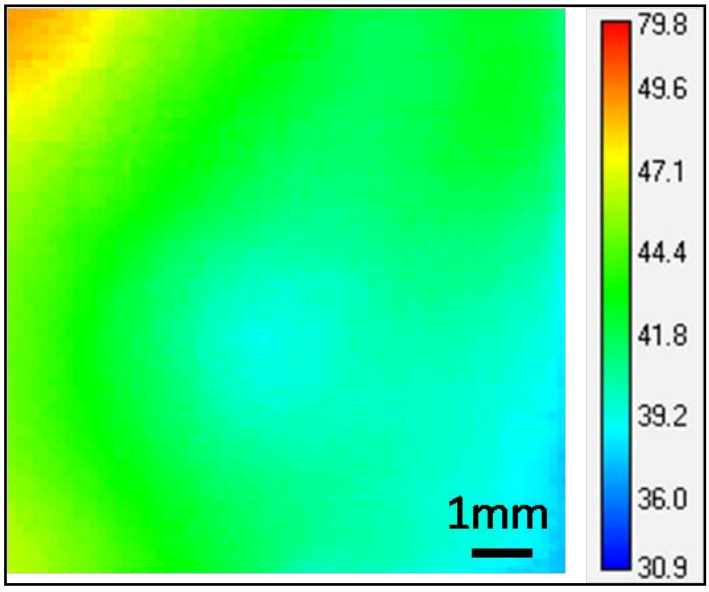

Fig. 16. Real-time IR image of nano-structured surface in the single droplet impingement cooling at high heat flux condition (19.8 W/cm^2)

4.2.2. Time-averaged thermal images of different surfaces

Time-averaged surface temperature profiles of different surfaces are shown in Fig. 17 and Fig. 18. Time-averaged thermal images are generated by using recorded temperature data (exported as comma separated value (.csv) file) and a MATLAB code. Each figure is based on averaged temperature data over 145 frames. Fig. 17 shows surface profiles for different surfaces at low heat flux condition while Fig. 18 shows the results at high heat flux condition.

The droplet impact points can be clearly seen on both of the figure. Also, the flow direction can be also identified by a lower temperature region outside the impact zone. The impact point is at a lower temperature than the flowing fluid downstream on the surface.

It is observed that time-averaged temperature gradients on the bare silicon surface are larger than on the nano-structured surface at both low and high heat fluxes. A smaller low temperature region in the impact zone can also be seen. This confirms that nano-structure features play a favorable role in film dynamics which results in better heat transfer performance.

However, a better way to quantify and understand the heat transfer characteristics of the two surfaces is by comparing temperature distributions at the impact zone, which will be discussed in the following sections.

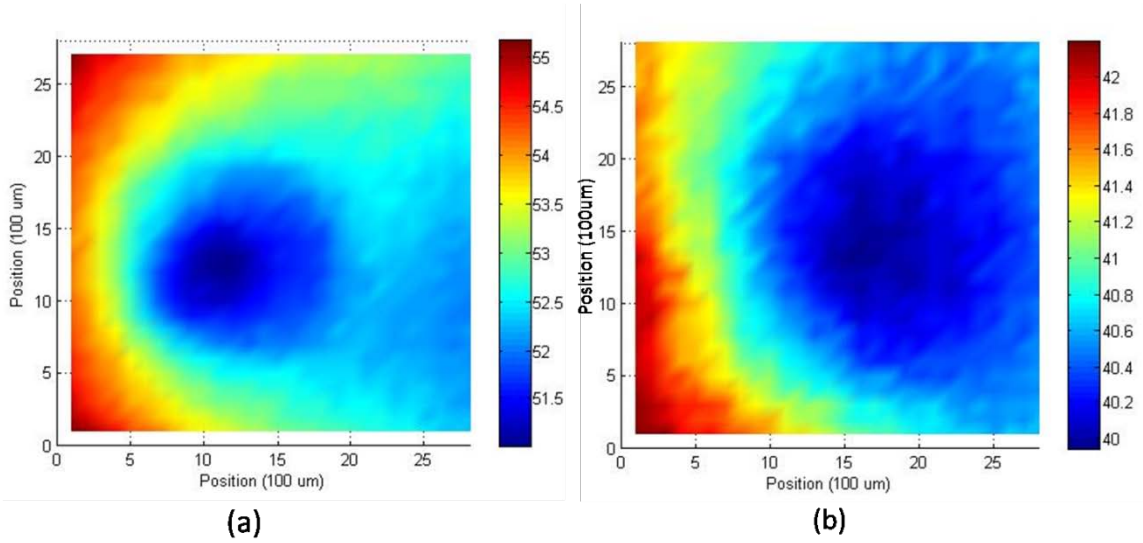

Fig. 17. Time-averaged temperature distribution on different surfaces at similar low heat flux condition near the impact zone in the single droplet impingement cooling (a) bare surface (19.7 W/cm^2), (b) nano-structured surface (19.8 W/cm^2)

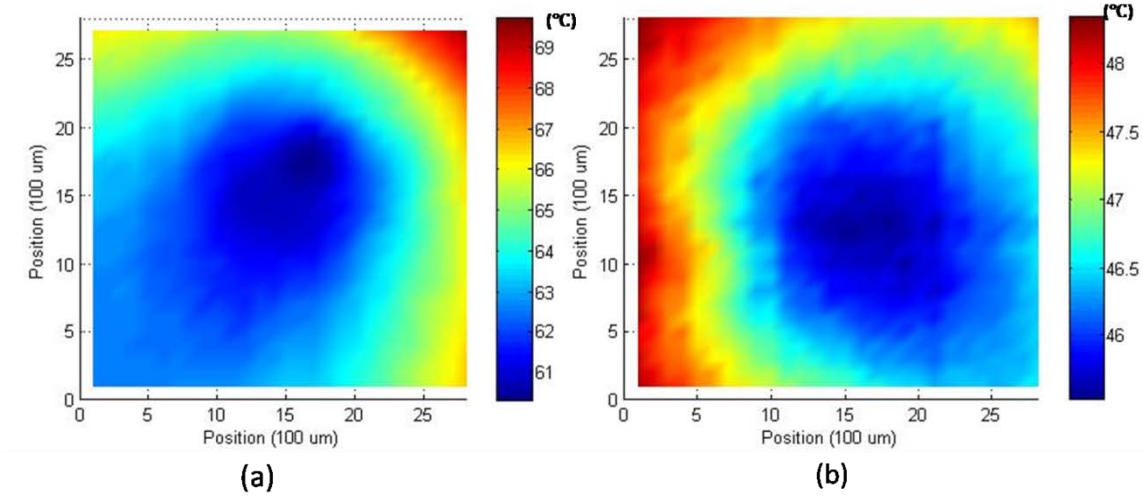

Fig. 18. Time-averaged temperature distribution on different surfaces at similar high heat flux condition near the impact zone in the single droplet impingement cooling (a) bare surface (26.4 W/cm^2), (b) nano-structured surface (26.9 W/cm^2)

4.2.3. Crown diameter measurement

Crown diameters were measured using a high speed camera and an image processing tool. A typical impact zone produced by impinging droplets can be seen in Fig. 19. It can be observed that the impact zone consists of two crown structures, a thinner film inside the impact crater with smoother film surface profile (defined as inner ring structure), and a thicker film on the edge of the impact crater with rugged film structure (defined as outer ring structure). Each diameter of the ring structures was measured at different heat flux values and listed Table 3 and Table 4 for different surfaces. Every listed crown diameter measurement was done by using the average value of forty high speed images.

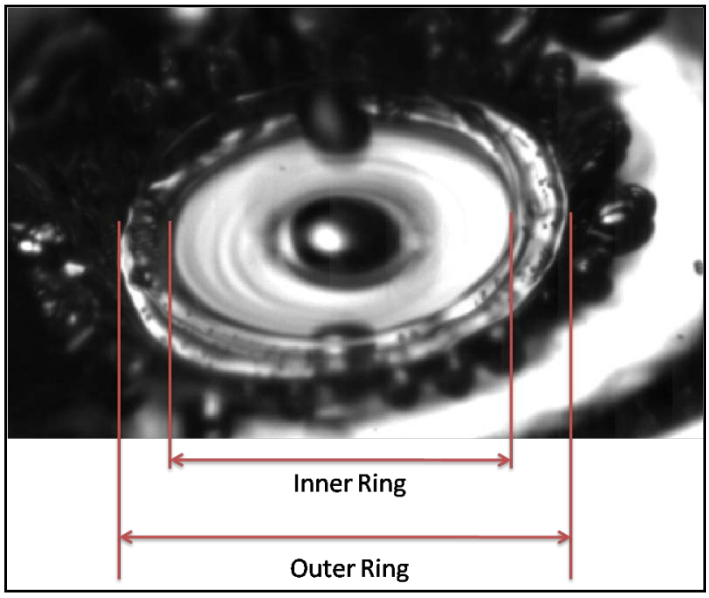

Fig. 19. High speed image of the impact zone and crown structures on the bare silicon surface in the single droplet impingement cooling experiment using FC-72 at 20 °C, 4500 Hz, 150 ml/hr under 9.7 W/cm^2

The high speed images of the impact crown for different surfaces at different heat flux conditions are shown in Fig. 20 to illustrate different impact crown behavior. The

high speed images suggest that the droplet cooling start deteriorating at a heat flux 21.7 W/cm^2 when a bare surface is used. Deterioration is noticeable when the liquid film outer ring structure within the impact crater starts breaking up. When the film break-up occurs then the impinging droplets can no longer sustain a complete ring structure. Fig. 20 (c) shows an image when the film starts breaking up. On the other hand, the nano-structured surface is able to maintain the outer ring structure at the same heat flux value. This is indicative of the effects of nanoscale features on film dynamics.

Table 3
Inner and outer ring diameter of the impact crown for bare silicon surface under different heat flux conditions

Bare silicon surface	Inner ring		Outer ring	
Heat Flux (W/cm^2)	Inner ring diameter, D_i (μm)	Standard deviation (μm)	Outer ring diameter, D_o (μm)	Standard deviation (μm)
9.5	1093.2	22.4	1439.8	24.7
16.1	1133.5	11.4	1334.1	25.0
21.7	1106.1	33.1	1203.6	23.5

Table 4
Inner and outer ring diameter of the impact crown for nano-structured surface under different heat flux conditions

Nano-structured surface	Inner ring		Outer ring	
Heat Flux (W/cm^2)	Inner ring diameter, D_i (μm)	Standard deviation (μm)	Outer ring diameter, D_o (μm)	Standard deviation (μm)
9.7	1055.8	26.9	1423.3	12.1
16.2	1040.8	37.5	1307.4	41.6
21.2	1135.4	47.5	1397.1	64.3

Inner and outer ring diameter data were plotted in Fig. 21 in order to clearly compare different crown behavior. It is observed that the relation between heat flux and inner ring diameter of both nano-structured and bare silicon surfaces are not significant. However, the size of the outer ring varied with heat flux when both nano-structured and bare surfaces were tested. The outer ring diameter of the bare silicon surface decreases with the increasing heat flux, which is not observed on the nano-structured surface. The data imply that the nano-structure surface helps sustain the crown structure at higher heat flux, and results in better cooling performance.

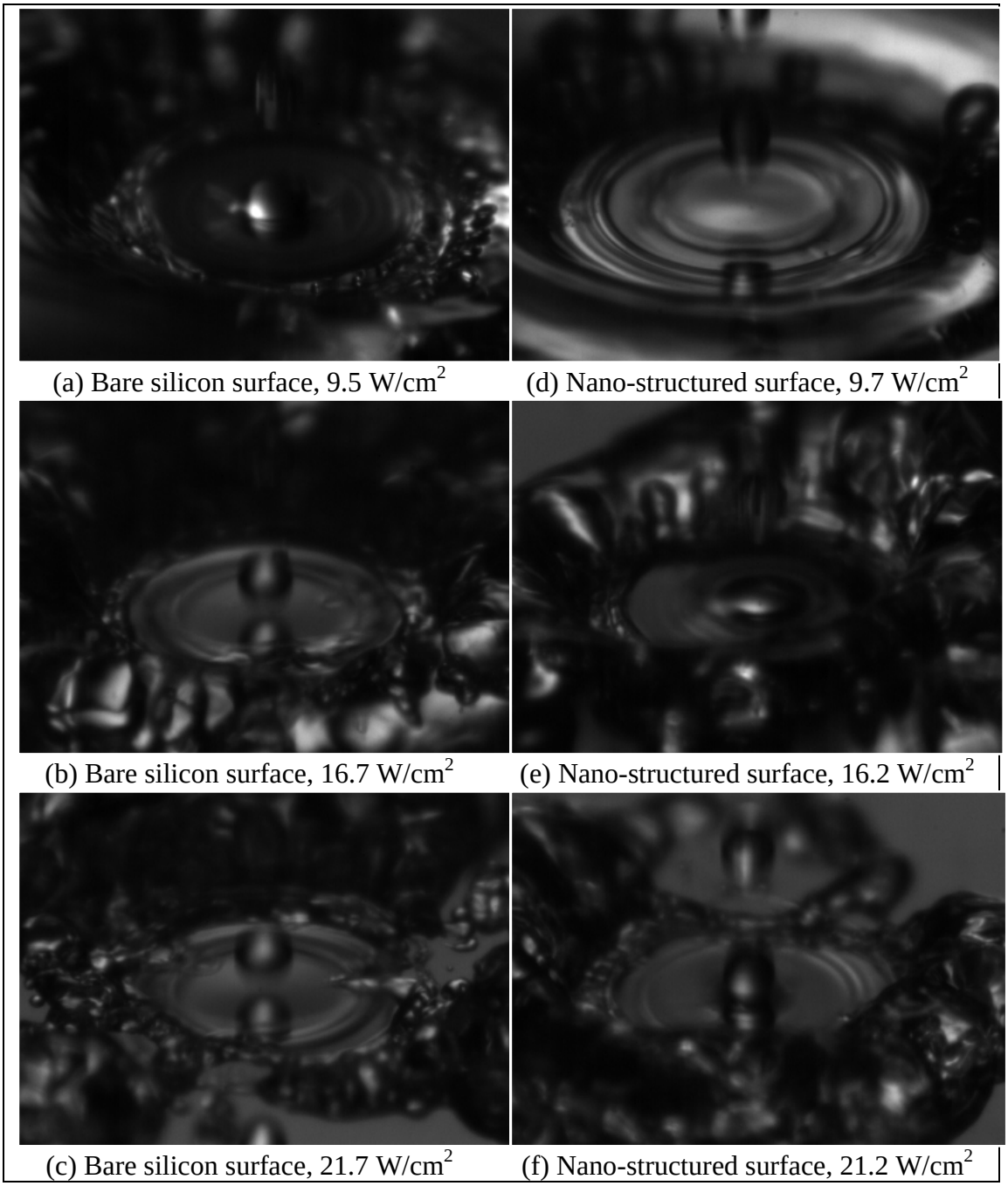

(a) Bare silicon surface, 9.5 W/cm^2 (d) Nano-structured surface, 9.7 W/cm^2

(b) Bare silicon surface, 16.7 W/cm^2 (e) Nano-structured surface, 16.2 W/cm^2

(c) Bare silicon surface, 21.7 W/cm^2 (f) Nano-structured surface, 21.2 W/cm^2

Fig. 20. High speed images of the impact crown on different surfaces under different heat flux conditions using FC-72 at 20 °C, 4500 Hz

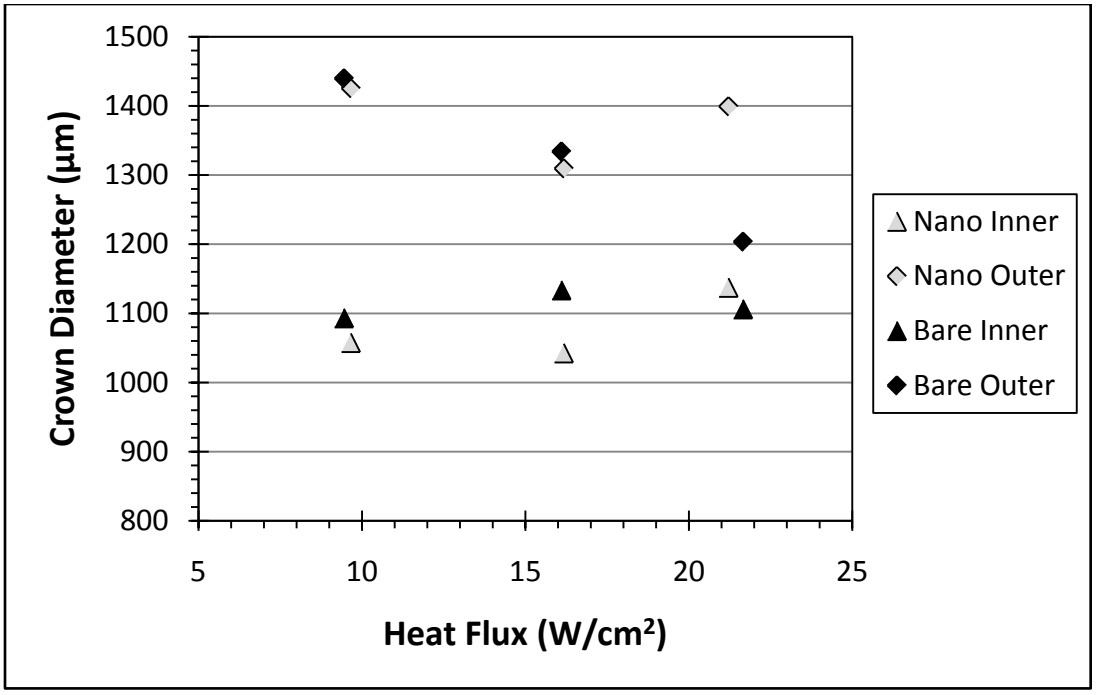

Fig. 21. Inner and outer ring diameter of the impact crowns on different surfaces in the single droplet impingement experiments under different heat flux conditions

Experimental results reveal that at a high heat flux condition, the nano-structured surface provides a larger thin film area (inner and outer ring structure) covered on the heater surface that efficiently allows for better heat removal from the heater surface. The ring structures of inner ring and outer ring also show different dynamic film topology that could explain the presence of an enhanced cooling mechanism.

To check on the possibility that the difference between outer and inner ring diameters (ΔD) could increase heat transfer, the ratio between ring diameter differences of the two surfaces ($\Delta D_n/\Delta D_b$) were calculated and listed in Table 5. It can be observed from Table 5 that there is an increase in the $\Delta D_n/\Delta D_b$ ratio with heat flux.

Table 5
Ring diameter difference (ΔD) data of different surfaces in the single droplet impingement experiments and ring diameter difference ratio ($\Delta D_n/\Delta D_b$)

Nano-Structured Surface		Bare Silicon Surface			
Heat Flux (W/cm^2)	Ring Diameter Difference, ΔD_n (μm)	Heat Flux (W/cm^2)	Ring Diameter Difference, ΔD_b (μm)	Averaged Heat Flux (W/cm^2)	$\Delta D_n/\Delta D_b$
9.5	368.1	9.7	346.6	9.6	1.062
16.2	267.1	16.1	200.6	16.2	1.332
21.2	262.1	21.7	97.5	21.5	2.689

Also, it can be seen that the ring diameter difference decreases with heat flux. However, it can be noticed that that nano-structured surface maintains a significant difference between outer and inner ring diameter. It can be concluded that the difference between outer and ring diameters (ΔD) and its corresponding film topology have a direct effect on surface temperature. Future work in this area will look at the topological factors responsible for enhanced cooling at high heat flux.

4.2.4. Minimum wall temperature (T_m)

4.2.4.1. Effect of fluid temperature

In this study, different fluid temperatures of 10 °C, 20 °C, and 30 °C were used to determine the effect of the fluid temperature on the single droplet impingement cooling. The results are shown in Fig. 22 and Fig. 23 for bare silicon surface and nano-structured surface, respectively using minimum wall temperature under different heat flux conditions.

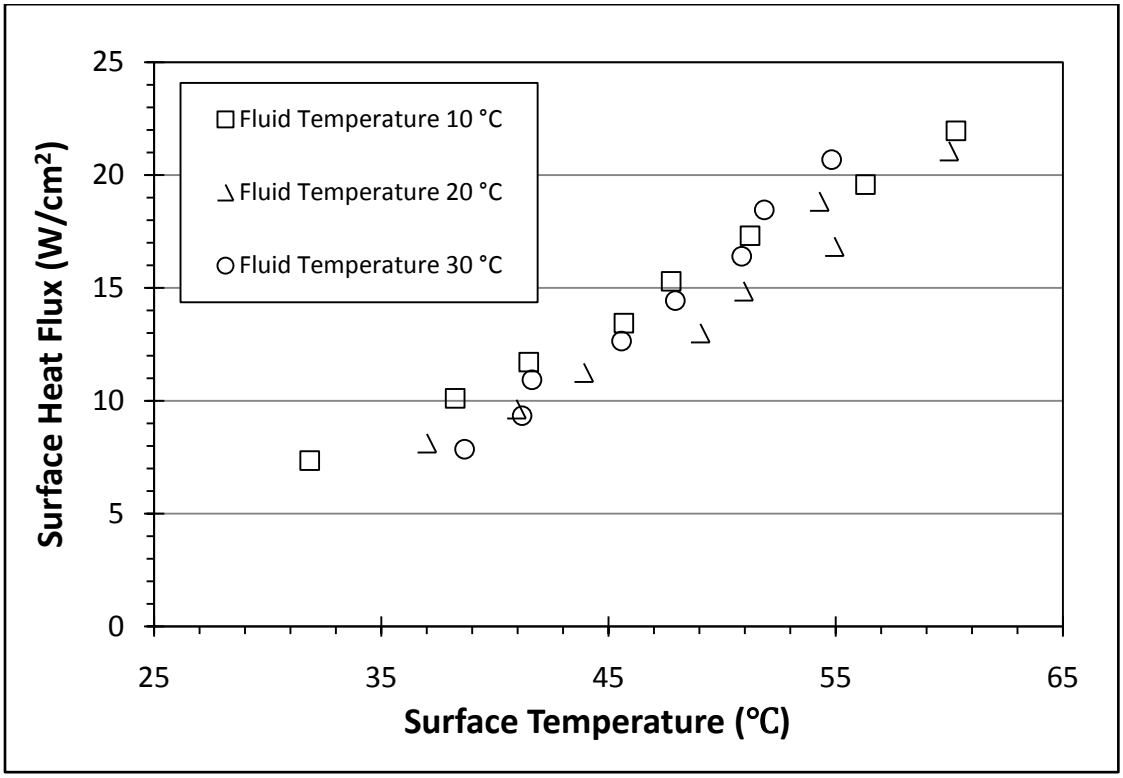

Fig. 22. Minimum wall temperature of the bare silicon surface for single droplet impingement experiments under different heat flux conditions using FC-72 with fluid temperature at 10 °C, 20 °C, and 30°C

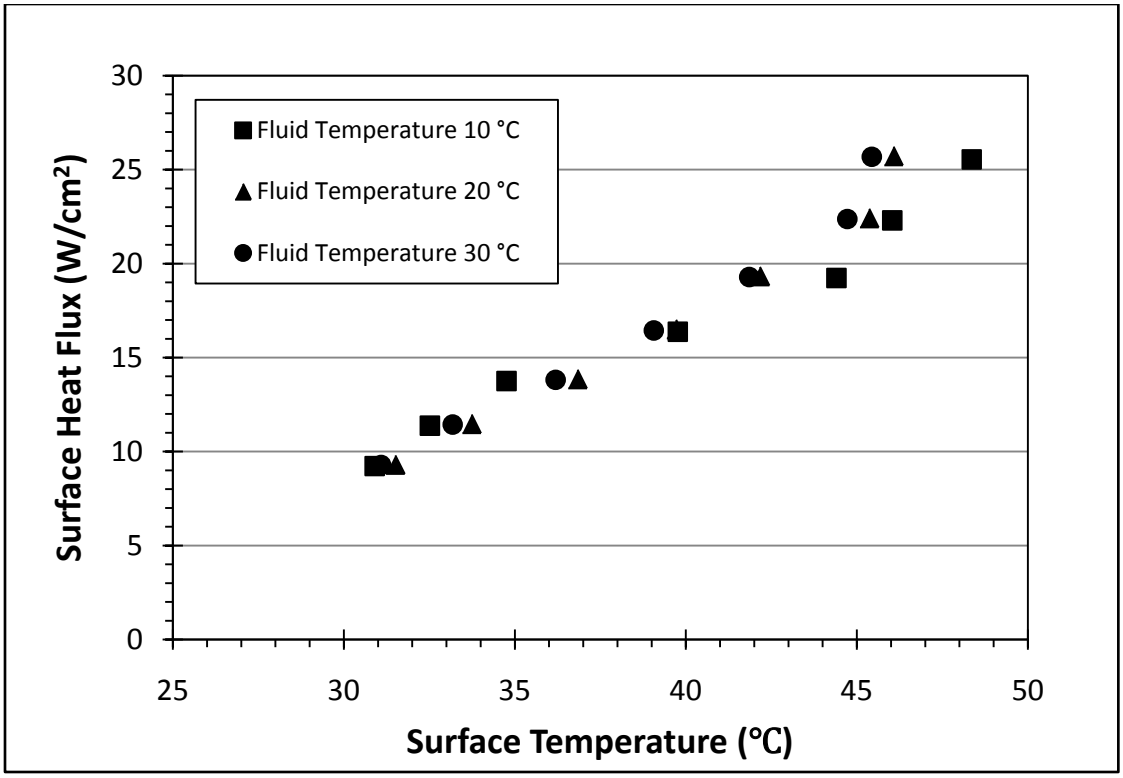

Fig. 23. Minimum wall temperature of the nano-structured surface for single droplet impingement experiments under different heat flux conditions using FC-72 with fluid temperature at 10 °C, 20 °C, and 30 °C

It is observed that the effect of fluid temperature is not significant. To understand that behavior, the first law equation is used to see if sensible cooling is a significant component in the heat transfer process. The first law equation in this case is as follows:

$$\dot{m} \times C_p \times \Delta T = q" \qquad (3)$$

Where $\dot{m}$ = fluid mass flow rate, C_p = liquid specific heat, and ΔT = temperature difference of the fluid before hits the surface and after existing the crown area. When substitute $\dot{m} = \rho \times \dot{V}$ into equation (3), following equation is obtained:

$$\rho \times \dot{V} \times C_p \times \Delta T = q" \quad (4)$$

Where ρ = fluid density and $\dot{V}$ = fluid volumetric flow rate. Using the properties of FC-72 and assuming $\triangle T$ = 10°C, 0.77 W is obtained. If the imposed heat flux is taken into account, FC72 should experience a much greater $\triangle T$ when it flows parallel to the surface and radial inside the impact crater. Therefore, a $\triangle T$ of 10 °C is not large enough to yield lower significantly better heat transfer. The data also suggest that heat transfer depends strongly on film dynamics than simply on fluid temperature. The data suggest that the effect the fluid temperature is a minor factor in the single droplet cooling experiments.

For each of the tests, a nearly linear increase of temperature under different heat flux can be observed as seen in Fig. 22 and Fig. 23. This suggests that single phase forced convection is the dominating heat transfer mechanism in the droplet impingement cooling since no two-phase behavior can be observed inside the impact zone.

4.2.4.2. Effect of surface structure

The heat transfer data of the nano-structured and bare surfaces are shown in Fig. 24. This figure shows the measured minimum wall temperature with respect to different heat flux conditions of the nano-structured surface as well as on the bare silicon surface. Fig. 24 contains 6 tests of nano-structured surfaces and 5 tests of bare silicon data.

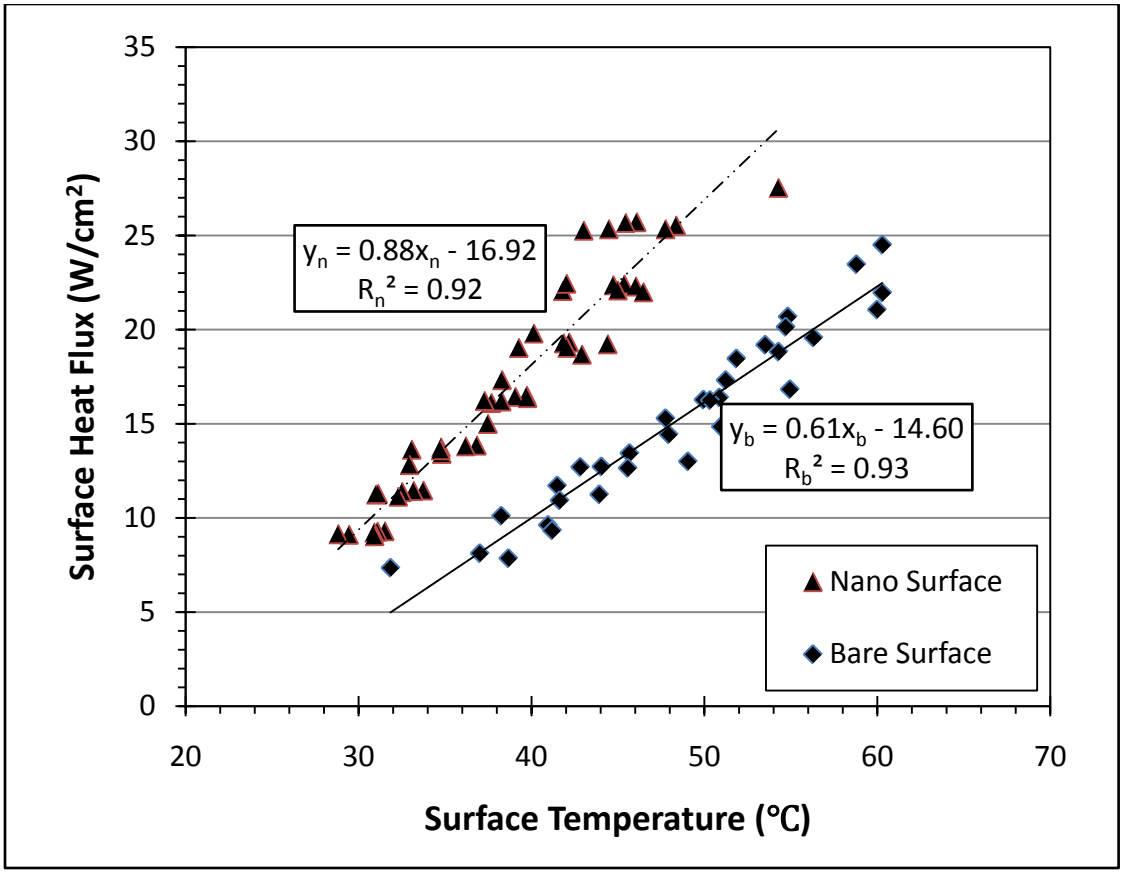

Fig. 24. Minimum wall temperature of different surfaces for single droplet impingement cooling under different heat flux conditions using FC-72

It is observed from Fig. 24 that both surfaces can dissipate heat flux close to 25 W/cm^2. Also, minimum wall temperatures are lower for the nano-structured surface than that for the bare silicon surface under the same heat flux values. Furthermore, the difference between surface temperature increases as heat flux increases indicating that heat dissipation in nano-structured surface is more significant. This is an evidence of a stronger heat transfer behavior when nano-structured surfaces are used, including the fact that there is a temperature difference of 20 °C between nano-structured and bare silicon surfaces at 25 W/cm^2.

A linear regression model was used to study the relationship between heat flux and its corresponding wall temperature for both cases, as shown in (5) and (6).

$$y_n = 0.88x_n - 16.93 \quad (5)$$

$$y_b = 0.61x_b - 14.60 \quad (6)$$

From (5) and (6), it is clear that the slope of nano-structured surface is significantly steeper (44.2% increase in slope), indicating the nano-structured surface has a better heat transfer performance. Furthermore, from residual analysis, the R^2 value in both cases is greater than 0.92 indicating a good correlation.

However, the minimum wall temperature can only be used to reveal the information at the impact points, which is not enough to explain different heat transfer mechanism on the heater surface. Therefore, radial temperature distributions near the impact zone are used to study the different behavior deep into the impact zone.

4.2.5. Radial temperature distribution near the impact zone

The heat transfer behavior of single droplet impingement cooling and the effect of using nano structures were also examined using radial temperature distribution in the impact zone. These distributions represent the temperature profiles that slice along the impact point, which provide much more information inside an impact crater. As in the previous section, each temperature point is a time-averaged value over 145 IR frames. The results are discussed below.

4.2.5.1. Bare silicon surface

The radial temperature distributions of the bare surface under different heat flux conditions are shown in Fig. 25. Zero in the x-axis represents the location of droplet impact. It is observed that the curves become steeper with the increasing heat flux. This indicates that the area at lower temperature caused by the droplet decreases with increasing heat flux.

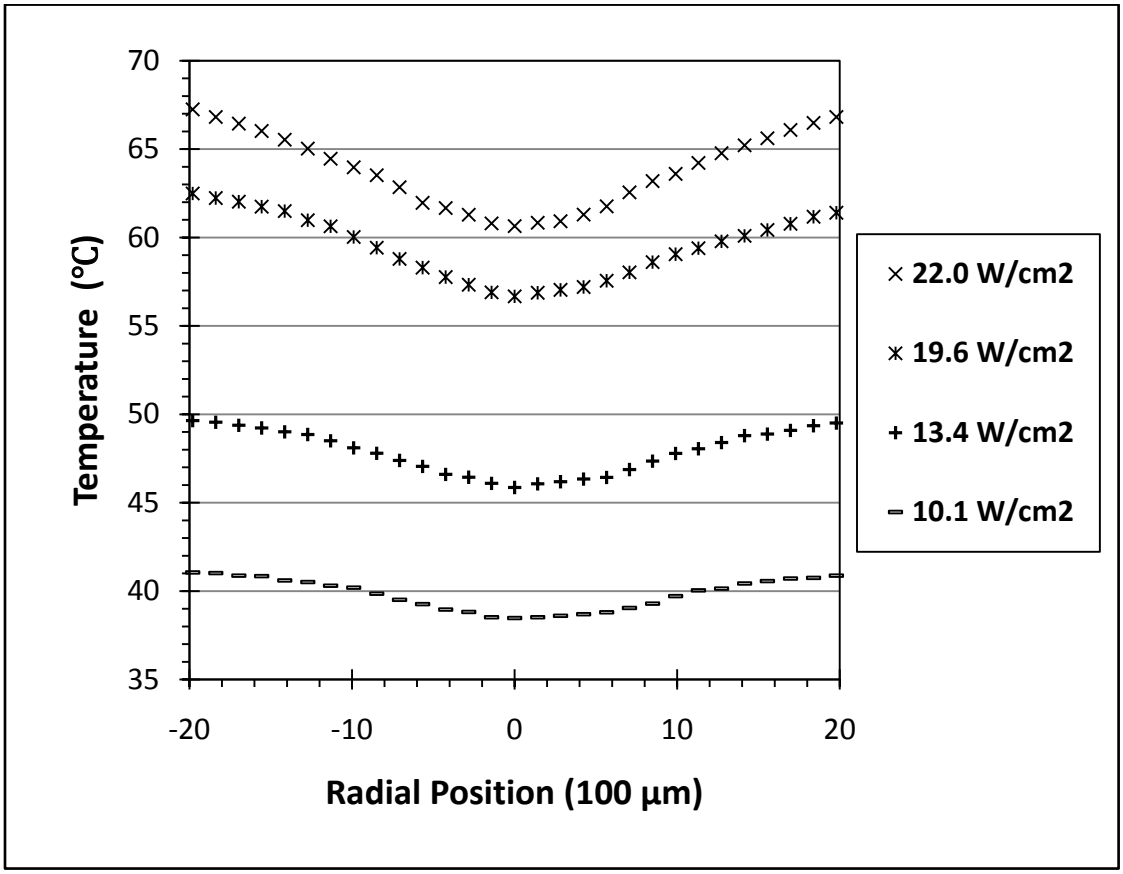

Fig. 25. Radial temperature distribution of the bare silicon surface for single droplet impingement cooling under different heat flux conditions using FC-72

A six order polynomial regression model was used to correlate heat flux to surface temperature (q'' vs. T_{sur}) on the bare silicon surface under different heat flux conditions. The curve was used to study the heat transfer behavior of the surface. Residual analysis shows that the correlation coefficient (R^2) was over 0.99 for all fitted regression models.

The inflection points of each curve (model) were obtained using secondary derivative analysis. The horizontal distance between the impact point (x = 0.0) and the inflection points were calculated and shown in the Table 6. This distance is defined as effective thermal diameter (d_e) in this study. It is assumed that thermal effective diameter based on inflection point is a good indication of the effect of heat flux on temperature distribution for each droplet stream because the impinging droplets cooling capability away from the effective diameter diminishes significantly as the temperature gradient reaches a maximum value and then become smaller after the inflection point.

For bare surfaces, the correlation between the effective thermal diameter and surface heat flux is not significant, although the radial temperature increases as the heat flux increases.

Table 6
Effective thermal diameter of the bare silicon surface for single droplet impingement cooling obtained using six order polynomial regression models

Heat Flux (W/cm^2)	Effective Thermal Diameter, d_e (μm)	Residual Analysis R^2 value
22.0	2121.6	0.99
19.5	1960.6	0.99
13.4	2107.7	0.99
10.1	2047.1	0.99

4.2.5.2. Nano-structured surface

The radial temperature distributions on the nano-structured surface under different heat flux condition are shown in Fig. 26. The origin of the x-axis represents the impact position of the droplet. The same trends observed for the bare silicon surface under different heat flux were found on the nano-structured surface (i.e. the temperature profile becomes steeper with the increasing heat flux).

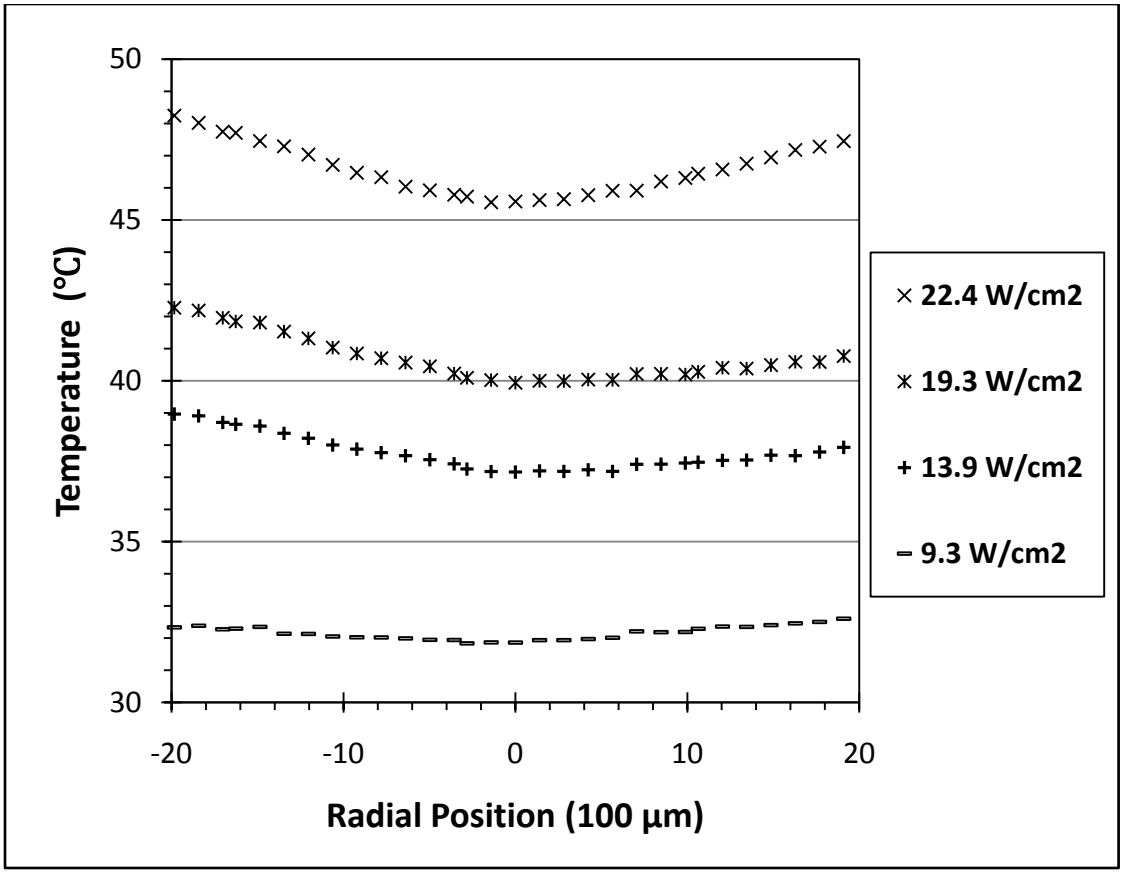

Fig. 26. Radial temperature distribution of the nano-structured surface for single droplet impingement cooling under different heat flux conditions using FC-72

Six-order polynomial regression model was also used to relate heat flux to surface temperature. Residual analysis shows that R^2 is over 0.97 for all the fitted regression models. The effective thermal diameter was obtained following the same method used in the previous section. Results are listed in Table 7. It can be observed that the effective thermal diameter increases with heat flux.

Table 7
Effective thermal diameter of the nano-structured surface for single droplet impingement cooling obtained using six order polynomial regression models

Heat Flux (W/cm^2)	Effective Thermal Diameter, d_e (μm)	Residual Analysis R^2 value
22.4	2900	0.998
19.3	2510	0.994
13.9	2420	0.992
9.3	2200	0.975

4.2.5.3. Comparison of bare and nano-structured surfaces

The temperature distribution on different surfaces under similar low and high heat flux conditions are shown in Fig. 27 and Fig. 28, respectively. It can be observed that the temperature profiles are more uniform for the nano-structured surface. In addition, the temperature difference between the two surfaces at the same radial location increases

with radial distance, indicating that the nano-structured surface results in better cooling. This implies that nano-structured surfaces result in the expansion of the cooling effect being brought by each impinging droplet.

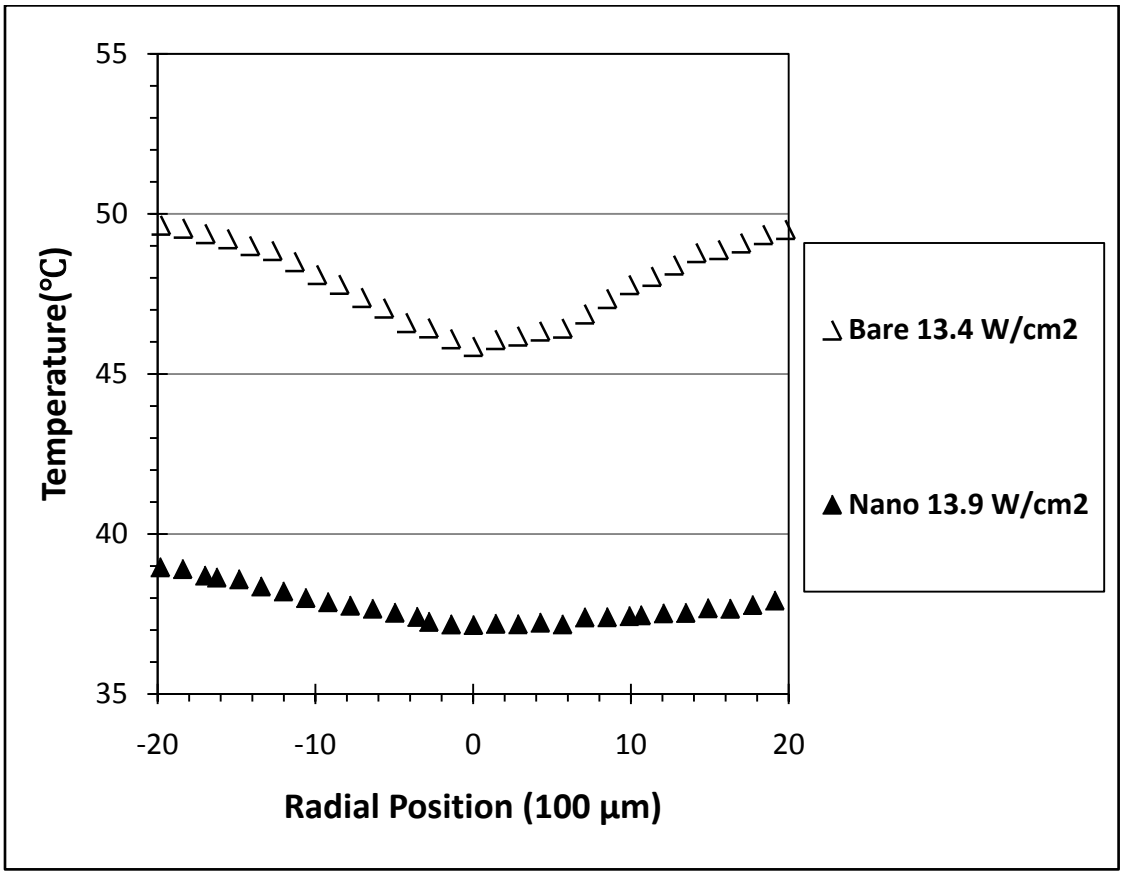

Fig. 27. Radial temperature distribution of different surfaces for single droplet impingement cooling at low heat flux conditions using FC-72

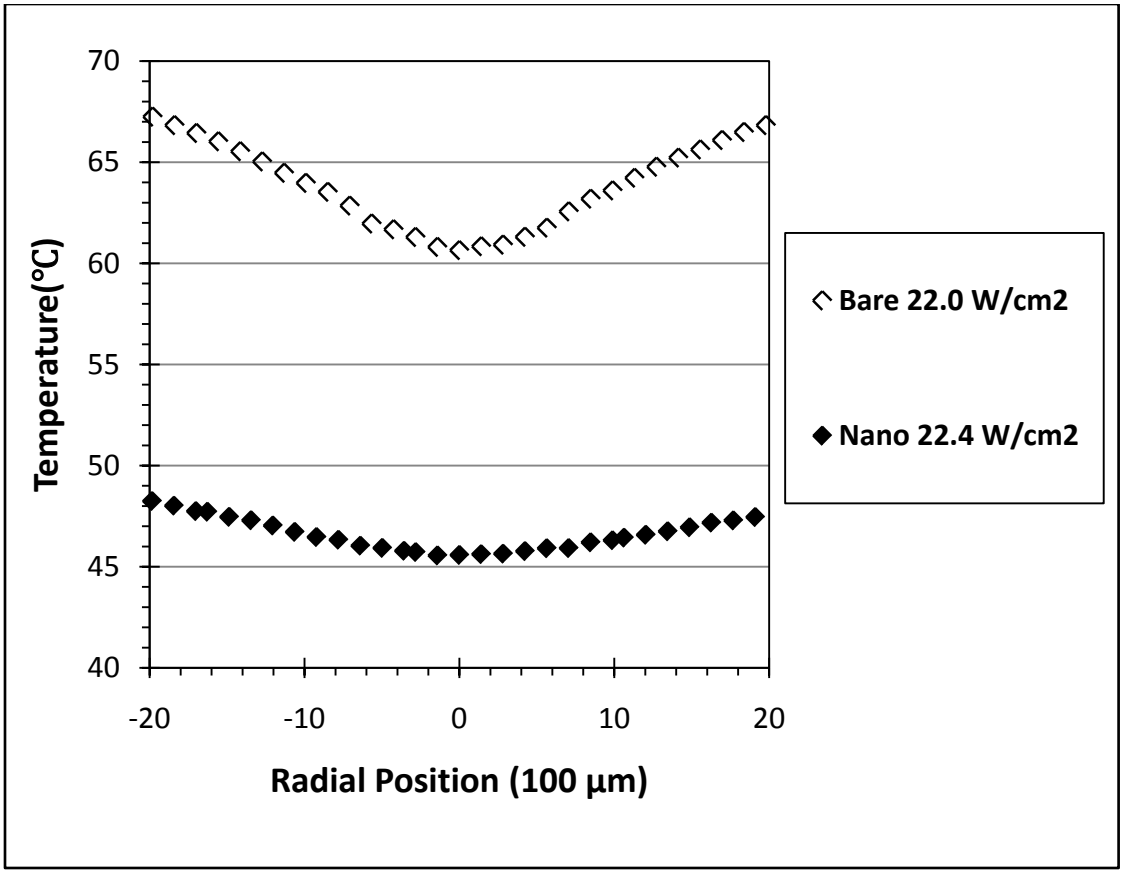

Fig. 28. Radial temperature distribution of different surfaces for single droplet impingement cooling at high heat flux conditions using FC-72

The effective thermal diameters on the bare silicon and nano structured surfaces for several heat flux values are compared and shown in Fig. 29. The figure shows how effective thermal diameter changes with heat flux. It can be seen that the effective thermal diameter of the nano-structured surface under similar heat flux condition is always larger than that of the bare silicon surface. Furthermore, the effective thermal

diameter of the nano-structured surface increases with the heat flux, while the effective thermal diameter of the bare silicon surface is more or less constant.

An increase in effective thermal diameter in the case of nano-structured surfaces is an indication of how the nano features induce a different liquid film dynamics leading to better heat transfer performance at higher heat flux values.

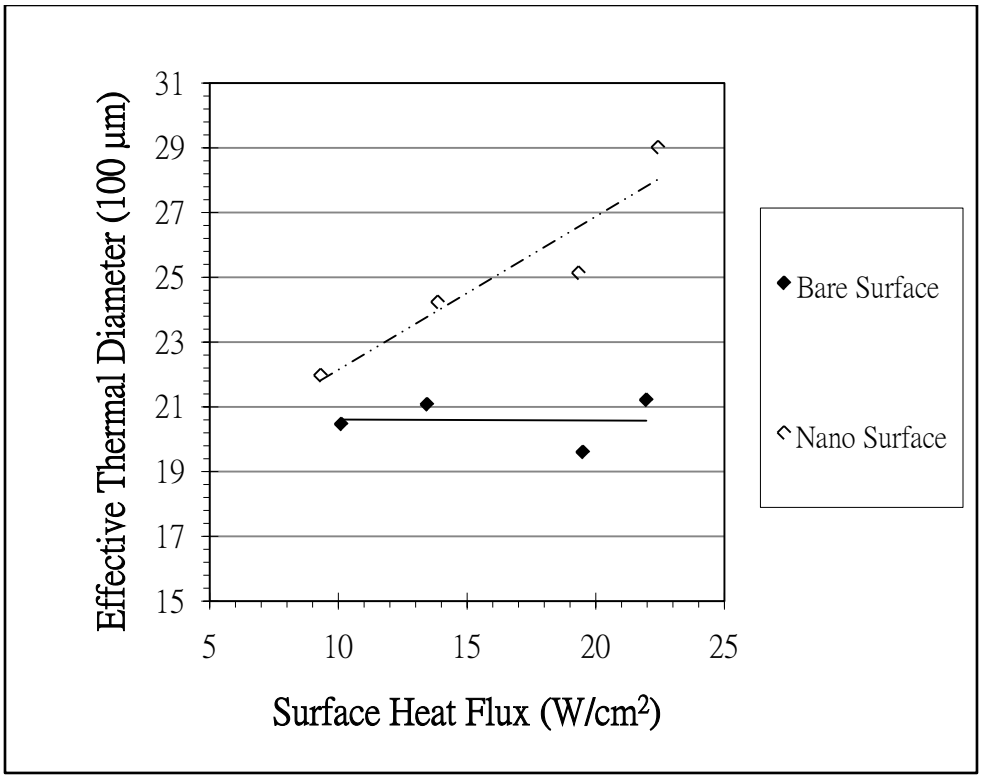

Fig. 29. Effective thermal diameters (d_e) of different surfaces for single droplet impingement cooling using FC-72, obtained using 6 order regression models under different heat flux conditions

4.3. Triple stream experiments

Triple stream cooling system experiments were conducted on different surfaces with two different stream spacing of 500 µm and 2000 µm. The stream spacing was defined as the distance between two adjacent droplet impact centers. Each spacing was tested twice on different surfaces to ensure good repeatability of the results. The results are presented and discussed using minimum wall temperature and radial temperature distribution near the impact zone in the following sections.

4.3.1. Minimum wall temperature

4.3.1.1. Effect of the surface structure

The effect of the surface structure on the triple stream experiments are shown in Fig. 30 and Fig. 31. Fig. 30 shows the results of two different surfaces with larger droplet stream spacing (2000 µm) while Fig. 31 shows the results for smaller droplet stream spacing (500 µm).

Larger droplet stream spacing

It is observed from Fig. 30 that with larger stream spacing (2000 µm), the nano-structured surface exhibits higher minimum wall temperatures at low heat flux conditions. After around 32 W/cm^2, the minimum wall temperature of the nano-structured surface is lower than the bare silicon surface. Also, the slope is larger which shows that the nano-structured surface has a better heat dissipation capability at high heat flux values.

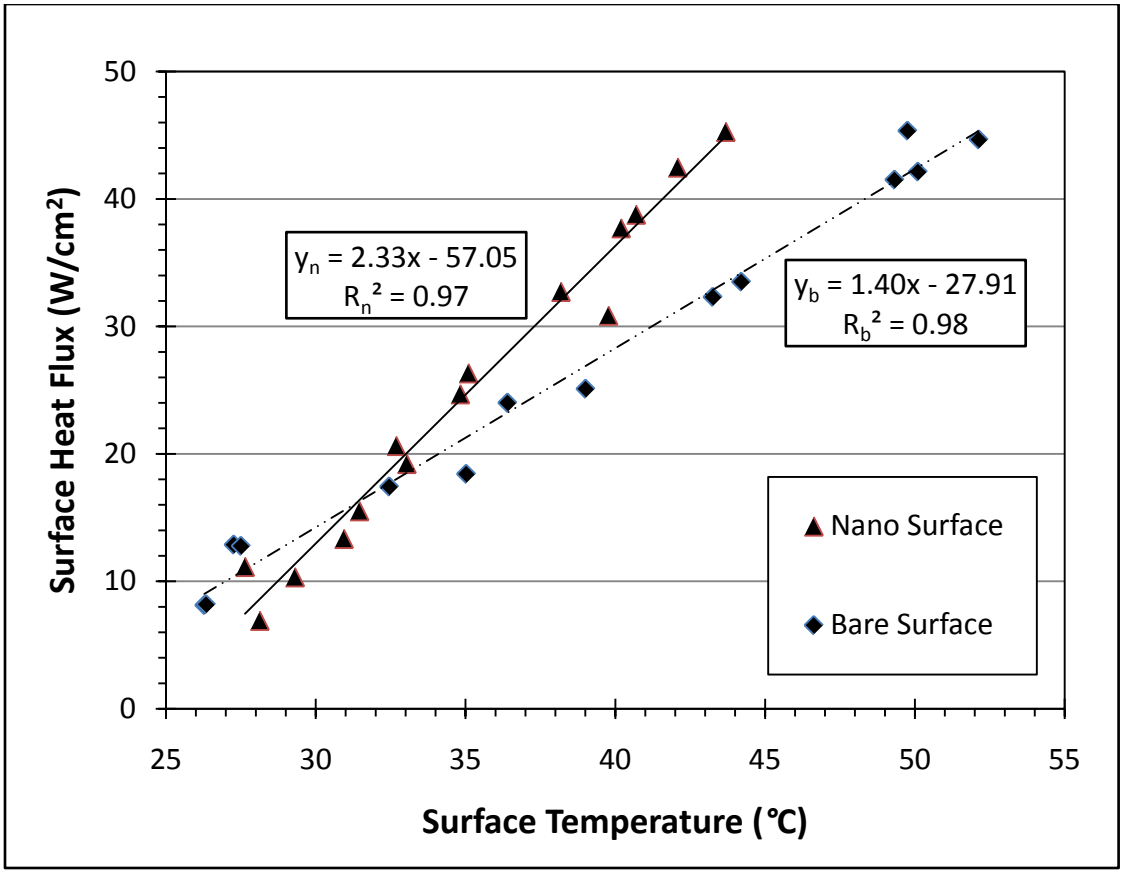

Fig. 30. Minimum wall temperature of different surfaces for triple droplet stream experiments with larger stream spacing (2000 µm) under different heat flux conditions using FC-72 at 20 °C

Smaller droplet stream spacing

Fig. 31 shows heat transfer data for smaller droplet stream spacing (500 µm). It is observed that the minimum wall temperature of nano-structured surface is lower than for the bare silicon surface. No crossover on minimum wall temperature was observed in this case. The figure shows that there is an approximately 5.5 °C temperature difference between two data sets.

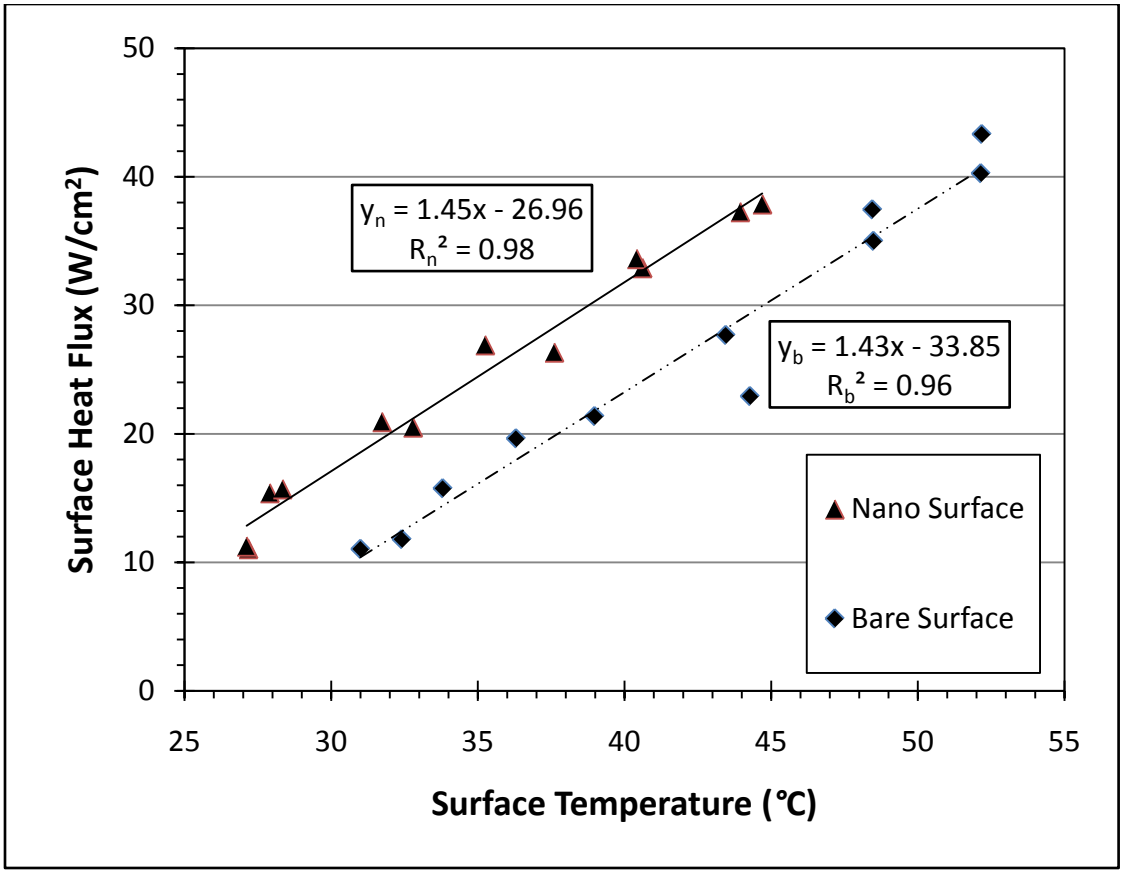

Fig. 31. Minimum wall temperature of different surfaces for triple droplet stream experiments with smaller stream spacing (500 µm) under different heat flux conditions using FC-72 at 20 °C

4.3.1.2. Effect of the stream spacing

The effect of different droplet stream spacing on the same surface is shown in Fig. 32 and Fig. 33. Fig. 32 and Fig. 33 show the results of two stream spacings (500 µm and 2000 µm) for bare silicon, and the nano-structured surface, respectively.

Bare silicon surface

It is observed from Fig. 32 that the minimum wall temperature of the bare silicon surface with a larger spacing (2000 µm) is slightly lower than with a smaller spacing

(500μm). Using a linear regression model, the slopes of the two curves shows a difference of less than 2.1% difference between each other.

Nano-structured surface

Fig. 33 shows that at low heat flux and larger spacing result in higher minimum wall temperature than with smaller spacing. With an increase in heat flux, there is a crossover effect between the two spacing when a nano-structured surface is used. After around 33 W/cm^2, the wall temperature is lower when using larger spacing than for the smaller spacing case, indicating that the heat transfer process is better at high heat flux values and larger spacings. Also, with increasing heat flux, the temperature difference between two spacing increases.

From the linear regression models, the curve slopes for the larger spacing case is larger than for smaller spacing case, which is indicative of an enhanced heat transfer process.

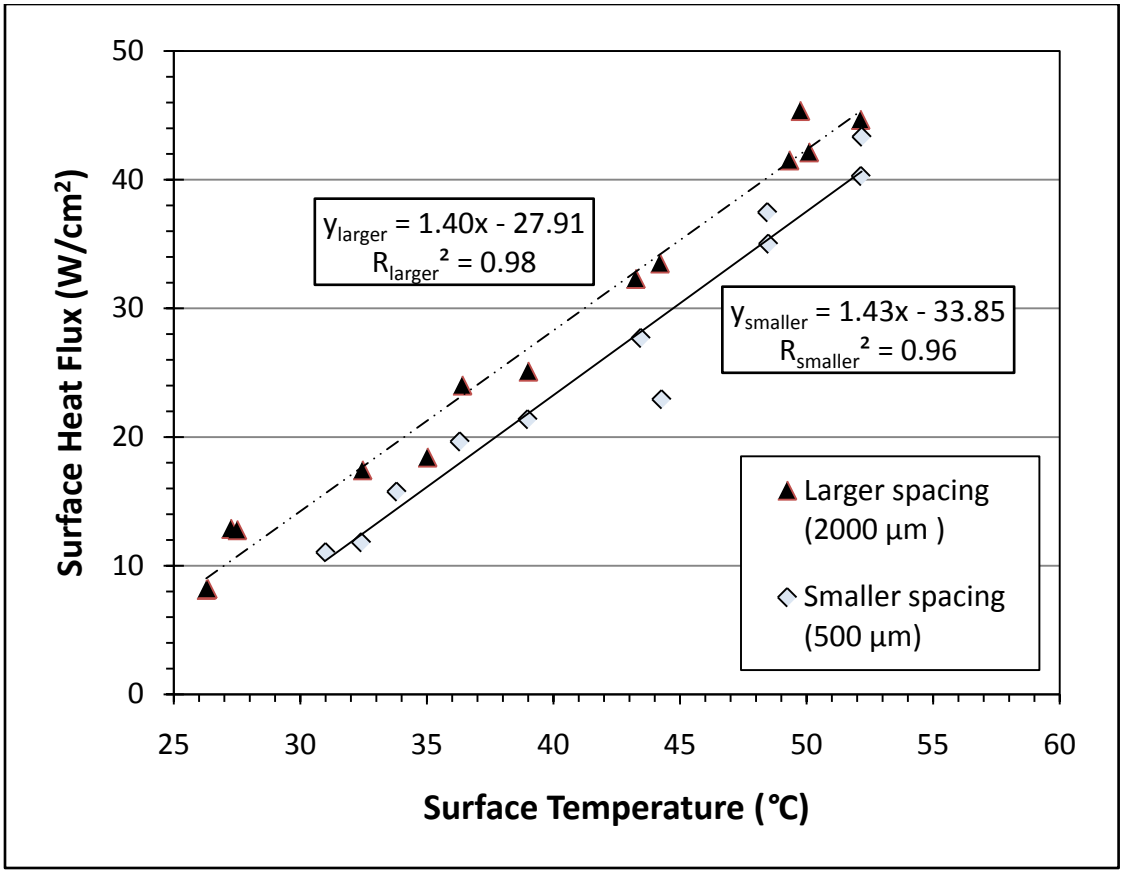

Fig. 32. Minimum wall temperature of bare silicon surface for triple droplet stream cooling with 500 µm and 2000 µm stream spacing under different heat flux conditions using FC-72 at 20 °C

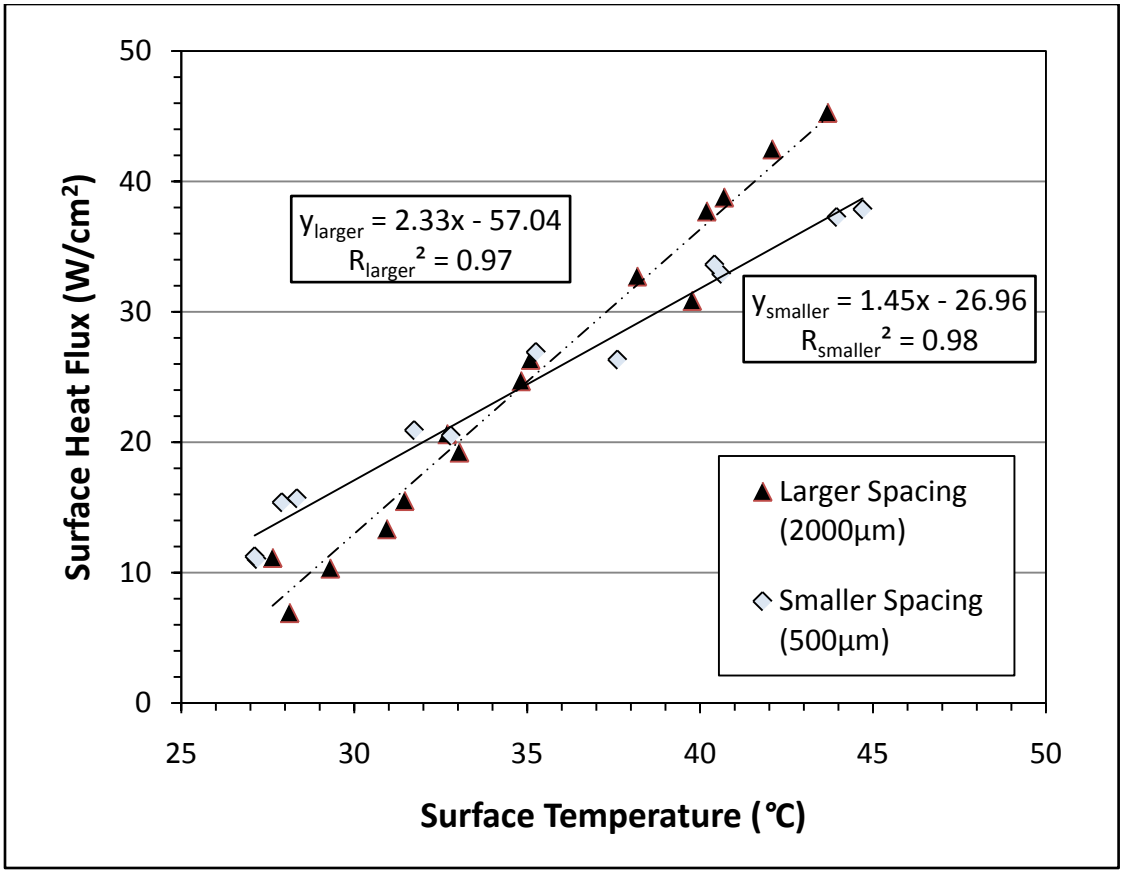

Fig. 33. Minimum wall temperature of nano-structured surface for triple droplet stream cooling with 500 µm and 2000 µm stream spacing under different heat flux conditions using FC-72 at 20 °C

4.3.1.3. Comparison of minimum wall temperature

From the results, it is observed that both bare silicon and nano-structured surfaces with larger droplet stream spacing maintain lower minimum wall temperatures at high heat flux conditions. However, changing impact droplet spacing and heat flux has a different effect on the nano-structured surface.

It is worth noticing that the slope of bare silicon surface case with spacings of 500 μm and 2000 μm and that of nano-structured surface with smaller spacing (500 μm) show very similar values with just a difference of 3.4%. This implies the heat transfer behavior of the nano-structure surface in the triple stream experiment with smaller stream spacing is very similar to the bare silicon surface case. In addition, it is observed that with triple stream cooling with larger stream spacing can reach higher heat flux conditions.

The slope of the nano-structured surface with larger droplet stream spacing is 61% higher than the slopes for other cases. This indicates that the heat transfer performance of the nano-structured surface with larger droplet stream spacing is far better. The proximity of adjacent droplets during smaller spacing experiments impact can suppress the enhanced film dynamics that the nano-structured surface seems to be inducing at larger spacing. This can also be proven by using the single droplet stream results where the measured crown diameters (larger than 1000 μm) are much larger than the droplet spacing (500 μm). Therefore there would be a deformation of the ring structure between neighboring crown structures that results in the reduction of the total crown area. The results confirm the crown structure plays an important role in the droplet impingement cooling especially in the multiple droplet stream system. Nevertheless, experimental

droplet cooling heat transfer performance for nano-structured surfaces is better than in bare surfaces even when using smaller spacing.

4.3.2. Radial temperature distribution near the impact zone

In this section, the effect of heat flux, spacing, and surface structure on radical temperature distribution are discussed.

4.3.2.1. Effect of different heat flux conditions

Bare silicon surface

Fig. 34 shows radial temperature distributions of the bare silicon surface for triple stream experiments with larger spacing (2000 μm) under different heat flux conditions. It is observed that the temperature at the impact points increases with heat flux. The temperature gradient also increases with heat flux. The points of impact can be clearly identified on the temperature distribution curve.

The radial temperature distributions for the bare silicon surface in the triple stream cooling with smaller spacing (500 μm) are shown in Fig. 35. Unlike the experiment with larger spacing, the impact points cannot be easily identified from the figure, leaving a

wide and flat low temperature region near the origin. It can also be observed that smaller steam spacing results in a different temperature profile. The data suggest that the film dynamics are affected adversely by bring impinging droplets closer together.

From Fig. 34 and Fig. 35, it can be seen that the surface temperature with larger droplet stream spacing is more uniform. However, stream with smaller spacing are better at cooling a specific locations.

Nano-structured surface

Fig. 36 and Fig. 37 show the radial temperature distribution of the nano-structured surface with a larger stream spacing (2000 μm) and smaller spacing (500 μm), respectively. The impact points of the droplet can still be seen in Fig. 36 although it is not as clear as in Fig. 34. In the smaller spacing experiments, Fig. 37 has the same characteristics as Fig. 35. It is shown that the temperature increases with increasing heat flux.

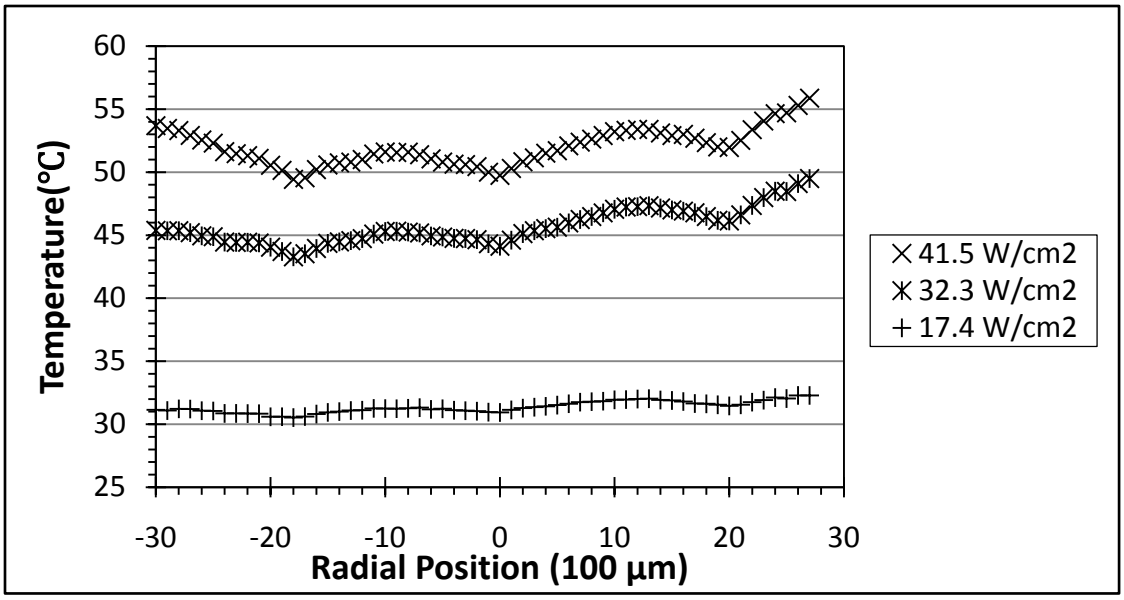

Fig. 34. Radial temperature distribution of the bare silicon surface for triple droplet stream cooling with larger stream spacing (2000 µm) at different heat flux conditions using FC-72 at 20 °C

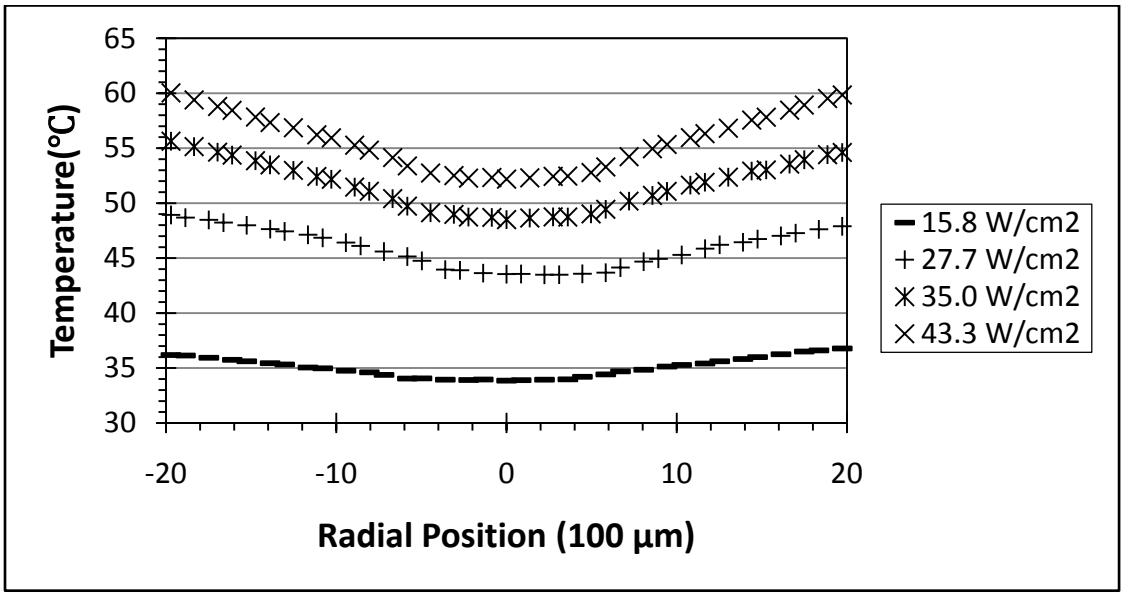

Fig. 35. Radial temperature distribution of the bare silicon surface for triple droplet stream cooling with smaller stream spacing (500 µm) at different heat flux conditions using FC-72 at 20 °C

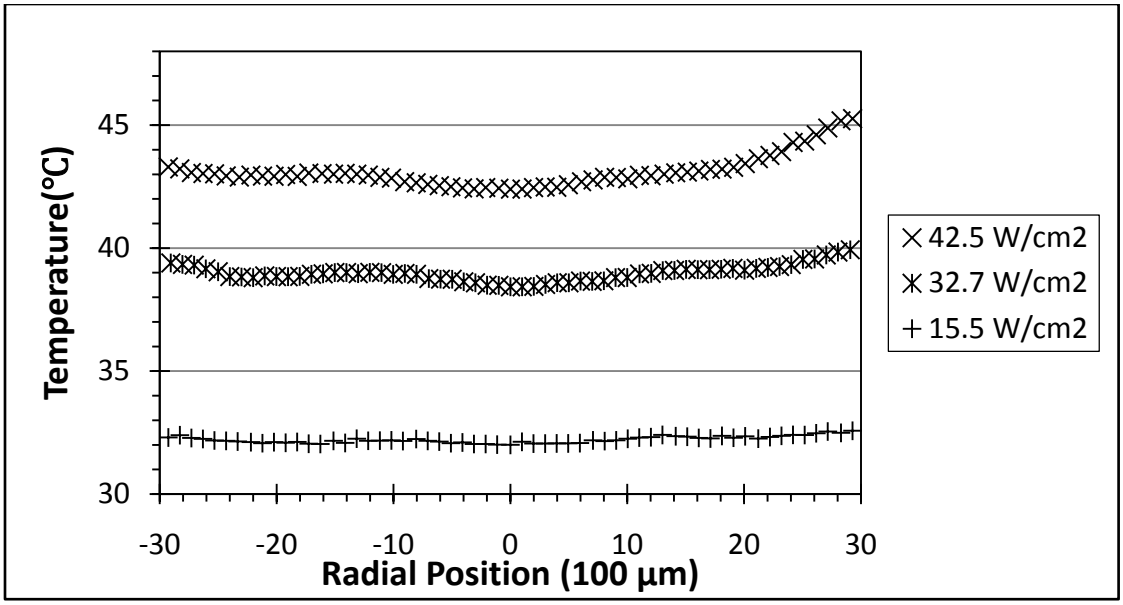

Fig. 36. Radial temperature distribution of the nano-structured surface for triple droplet stream cooling with larger stream spacing (2000 µm) at different heat flux conditions using FC-72 at 20 °C

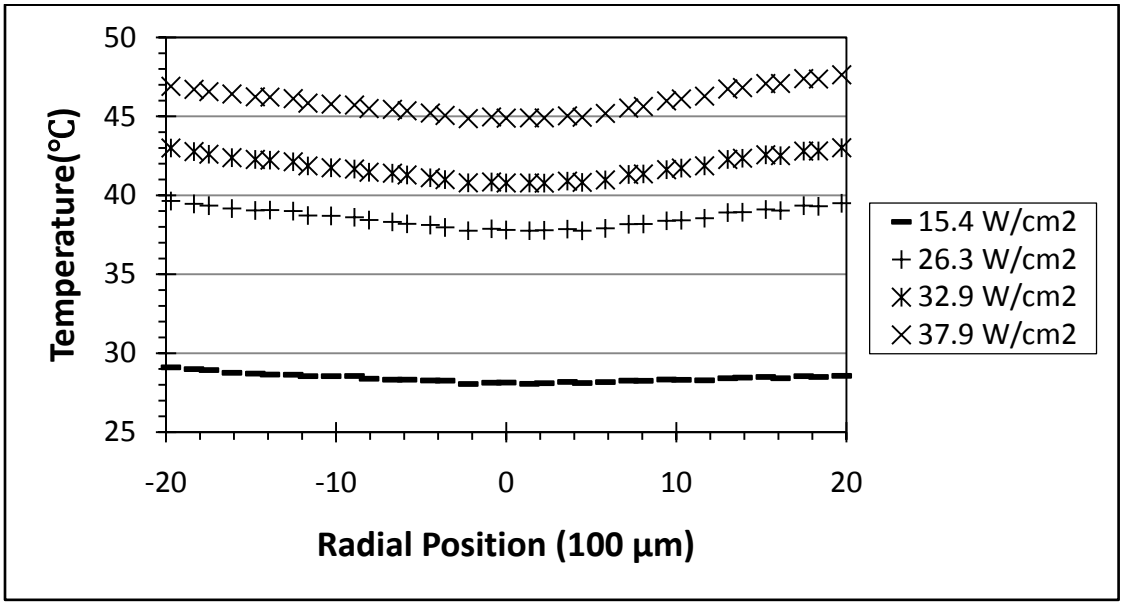

Fig. 37. Radial temperature distribution of the nano-structured surface for triple droplet stream cooling with smaller stream spacing (500 µm) at different heat flux conditions using FC-72 at 20 °C

Effective thermal diameter analysis

In smaller stream spacing (500 μm) experiments, both of the surfaces show similar temperature distribution characteristics to the single droplet stream results. Therefore, effective thermal diameter (d_e) analysis based on heat transfer data were done for bare silicon and nano-structured surfaces results. The effective thermal diameter results for bare silicon surface are listed in Table 8 and show the same characteristics as in the single droplet stream case. Effective thermal diameter on the bare silicon surface with smaller stream spacing does not change with heat flux. Also, compare to the single steam results, the effective thermal diameter is not significant larger, which indicates that intensive cooling only affects a small area and affected by the crown area (surface that covered with thinner film).

The same analysis was done on the nano-structured surface tested in triple stream experiment with smaller stream spacing at low and high heat flux conditions. Table 9 shows that the effective thermal diameter no longer changes with heat flux as seen in the case of single droplet stream. This implies that the heat transfer behavior in the impact zone of a nano-structured surface is similar to that of a bare silicon surface when the spacing is reduced. It is assumed that the suppression on the crown structure in this case is more severed for nano-structured surface where a larger outer ring structure was found in the single stream experiments. The break-up of the outer ring structure on the nano-structured surface results in similar heat transfer behavior to the bare silicon surface. This result also confirms the suggestion that larger outer ring structure is responsible for better heat transfer performance on the nano-structured surface.

Table 8
Effective thermal diameter of the bare silicon surface for triple droplet stream impingement cooling obtained using six order polynomial regression models

Heat Flux (W/cm^2)	Effective Thermal Diameter, d_e (μm)	Residual Analysis R^2 value
43.3	2300	0.99
35.0	2130	0.99
27.7	2010	0.99
15.8	2110	0.99

Table 9
Effective thermal diameter of the nano-structured surface for triple droplet stream impingement cooling obtained using six order polynomial regression models

Heat Flux (W/cm^2)	Effective Thermal Diameter, d_e (μm)	Residual Analysis R^2 value
39.7	2140	0.99
15.4	2220	0.97

4.3.2.2. Effect of surface structure

Fig. 38-40 are used to show the behavior of different surfaces (bare silicon and nano-structured surfaces) under the same spacing and heat flux condition. Fig. 38 and Fig. 39 show low heat flux conditions with two different stream spacing; Fig. 40 and Fig. 41 show the high heat flux conditions with two different spacing.

A comparison of radial temperature distribution on different surfaces with larger spacing (2000 μm) under similar low heat fluxes condition is shown in Fig. 38. It is observed that the temperature of the nano-structured surface is higher than on bare silicon surface at the given heat flux. The temperature profile on the nano-structured surface is more uniform than bare silicon surface.

Fig. 39 shows a comparison of radial temperature distribution for different surfaces with smaller spacing (500 μm) under similar low heat fluxes. The temperature of the nano-structured surface is lower than that of the bare silicon surface. Also, the temperature distribution is more uniform on the nano-structured surface.

Fig. 40 and Fig. 41 show the temperature profile of different surface under similar high heat flux conditions with larger and smaller stream spacing, respectively. It is observed in Fig. 40 that the temperature of the nano-structured surface is lower than bare silicon surface in this case. The temperature distribution is more uniform on the nano-structured surface at high heat flux when a temperature variation in the observed region is less than 2 °C for nano-structured surface and 5 °C for bare silicon surface.

Fig. 41 shows the radial temperature distributions with smaller spacing (500 μm) under similar high heat fluxes for different surfaces. As observed in the low heat flux case, the temperature profile of the nano-structured surface is lower and flatter. The temperature gradient increases more drastically for the bare silicon surface than for the nano-structured surface outside the impact area.

The results show that the nano structure ensures a more uniform temperature distribution on the surface with the nano-structured surface also shows a much better temperature profile outside the impact zone including a smaller temperature gradient outside the impact zone. Furthermore, the temperature profile for each impact point when using larger spacing has the same characteristics as in the single droplet impingement cooling experiments. This also indicates that at larger spacings, the heat transfer mechanisms seem to be independent of other impinging droplet as long as a nanostructured surface is used.

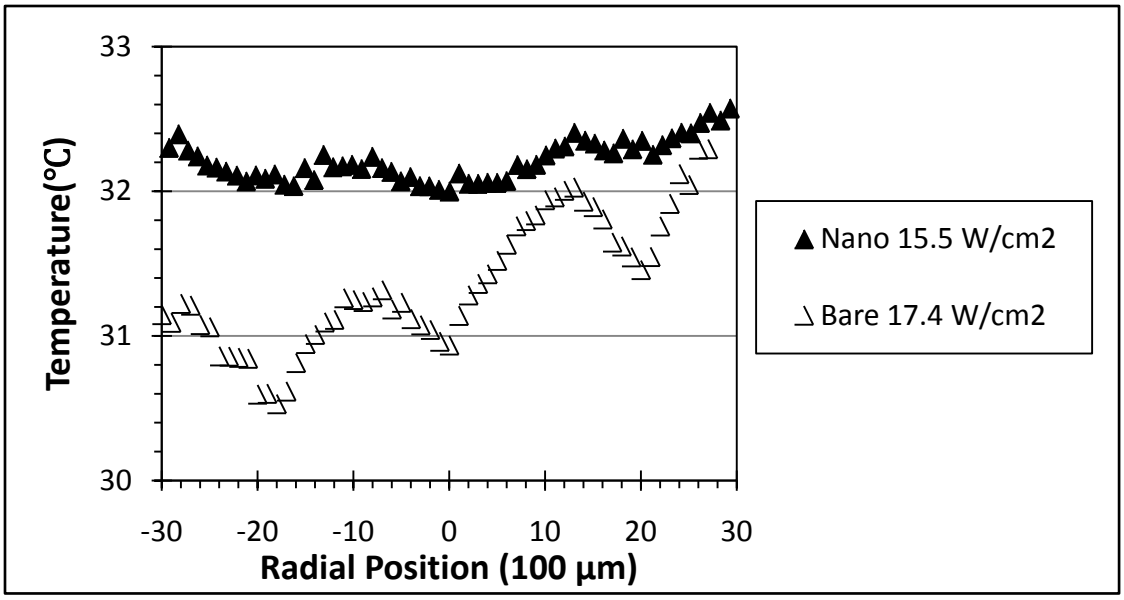

Fig. 38. Radial temperature distribution of different surfaces for triple droplet stream cooling with larger stream spacing (2000 µm) at low heat flux conditions using FC-72 at 20 °C

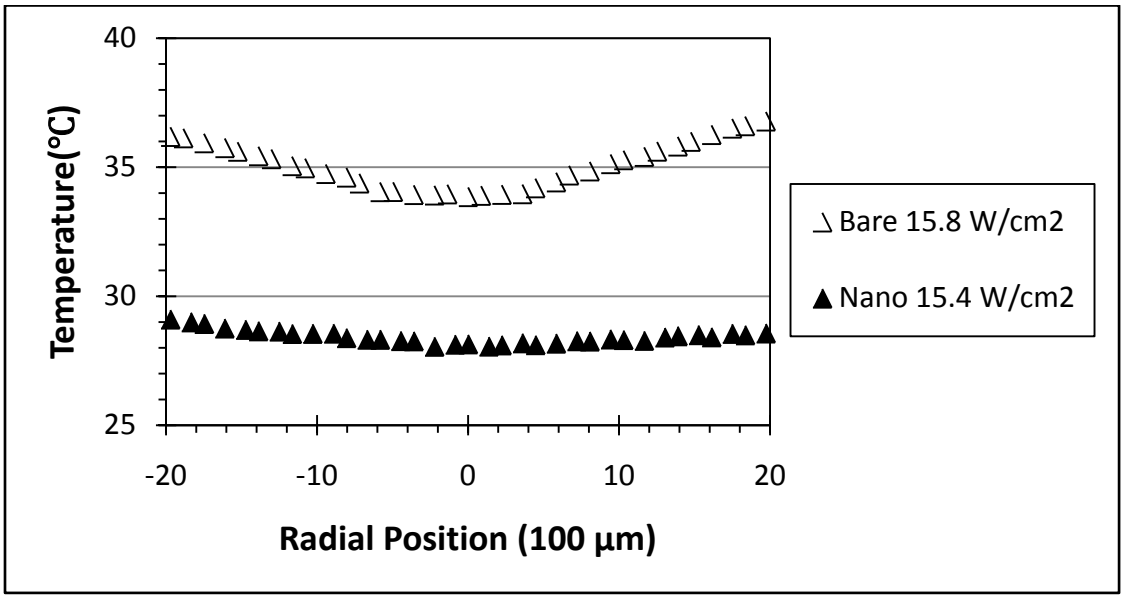

Fig. 39. Radial temperature distribution of different surfaces for triple droplet stream cooling with smaller stream spacing (500 µm) at low heat flux conditions using FC-72 at 20 °C

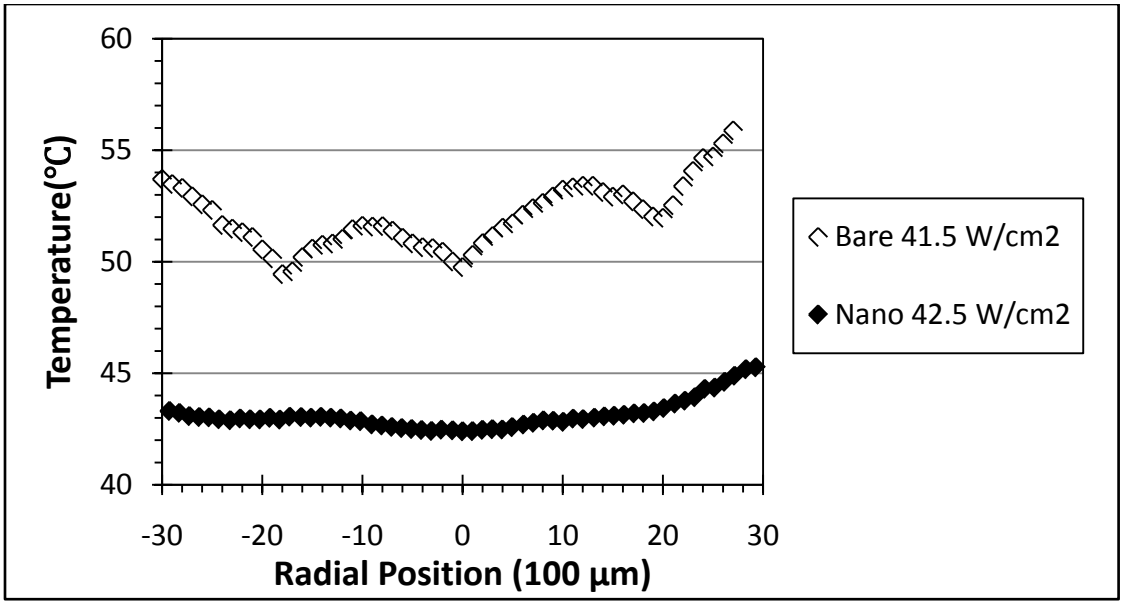

Fig. 40. Radial temperature distribution of different surfaces for triple droplet stream cooling with larger stream spacing (2000 µm) at high heat flux conditions using FC-72 at 20 °C

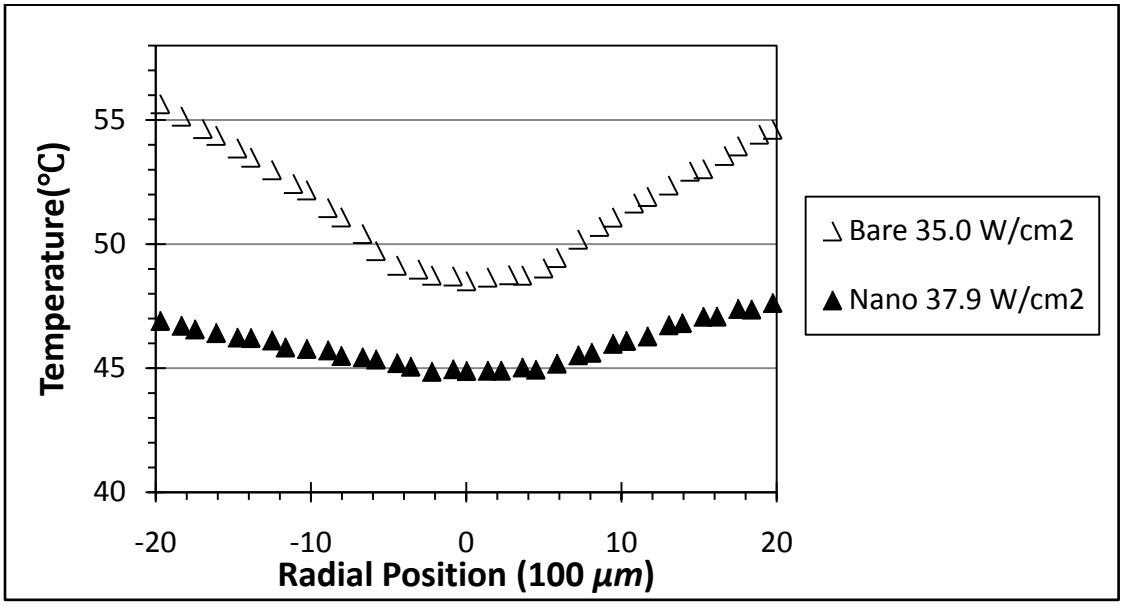

Fig. 41. Radial temperature distribution of different surfaces for triple droplet stream cooling with smaller stream spacing (500 µm) at high heat flux conditions using FC-72 at 20 °C

4.3.2.3. Effect of different stream spacing

Fig. 42-44 show the temperature response of the same surface to two stream spacing (500 µm and 2000 µm). Low heat flux conditions for bare silicon and nano-structured surfaces are shown in Fig. 42 and Fig. 43, respectively, and high heat flux conditions for bare silicon and nano-structured surface are shown in Fig. 44 and Fig. 45.

Bare silicon surface with different stream spacing (500 µm and 2000 µm) under similar low heat flux conditions is shown in Fig. 42. It is observed that the bare silicon surface with larger droplet stream spacing maintains lower temperatures in the impact zone. The temperature distribution on the surface is more uniform on the surface with a larger spacing.

The nano-structured surface with different stream spacing (500 µm and 2000 µm) under similar low heat flux conditions is shown in Fig. 43. In this case, higher temperatures are found with larger spacing on the nano-structured surface, which is different from the bare surface. Both spacing have good temperature uniformity on the surface. However, the profile for larger spacing is also slightly better.

Fig. 44 shows the temperature profile of the bare silicon surface under similar high heat flux conditions. It is also observed that the bare silicon surface with larger droplet

stream spacing holds lower temperature in the impact zone. The nano-structured surface temperature profiles with different stream spacing under high heat flux conditions are shown in Fig. 45. As observed on the bare silicon surface, the temperature profile is more uniform for larger spacing. However, the temperature difference between two different spacing profiles is only slightly larger than at lower heat flux.

The results in this section shows that the surfaces with larger droplet stream spacing (2000 μm) also has a larger area which results in a more even temperature distribution profile on the surface. This is good for large area cooling where heat is generated on the entire surface. On the other hand, the surface with a smaller spacing (500 μm) can provide a flat and wide temperature distribution in the impact zone, eliminating the temperature gradient that has been shown in the larger spacing. This shows that smaller spacing between droplet streams can provide a more intensive cooling in a small area.

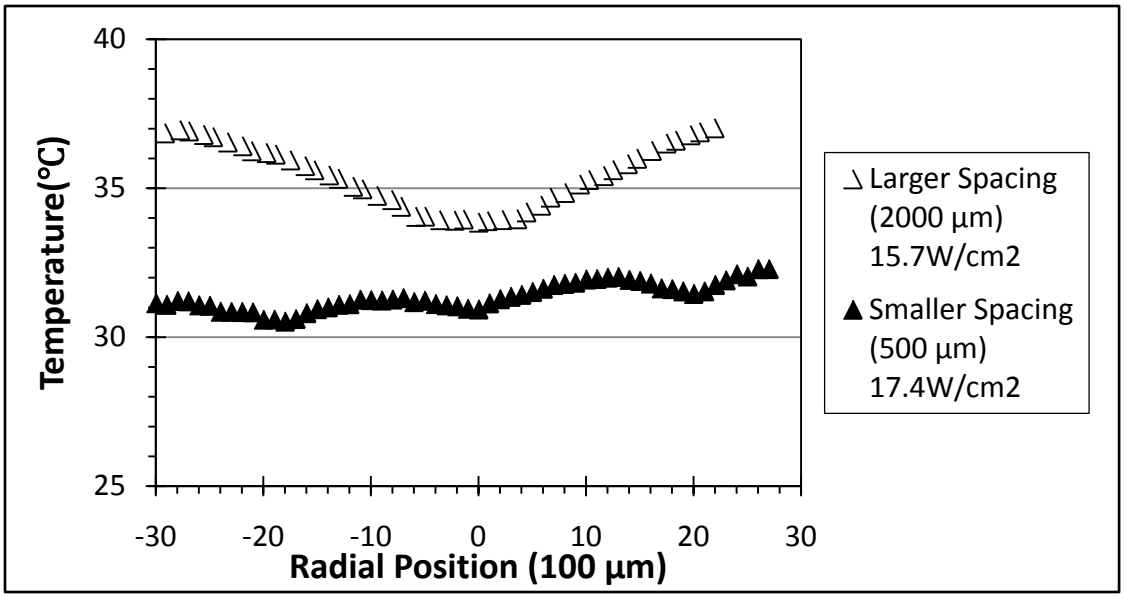

Fig. 42. Radial temperature distribution of the bare silicon surface for triple droplet stream cooling with different stream spacing (500 µm and 2000 µm) at low heat flux conditions using FC-72 at 20 °C

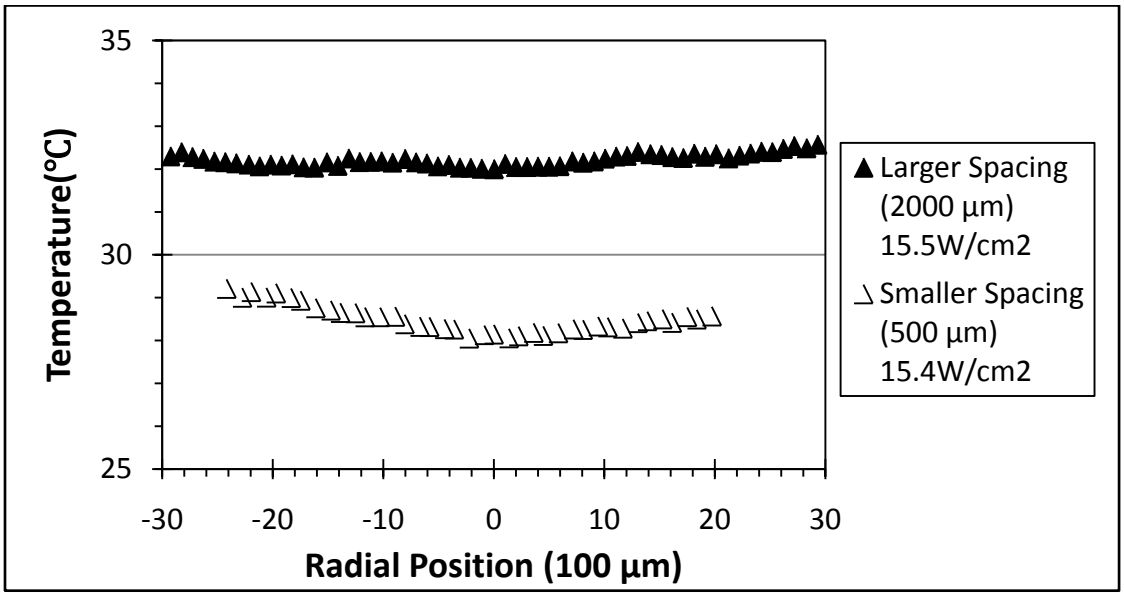

Fig. 43. Radial temperature distribution of the nano-structured surface for triple droplet stream cooling with different stream spacing (500 µm and 2000 µm) at low heat flux conditions using FC-72 at 20 °C

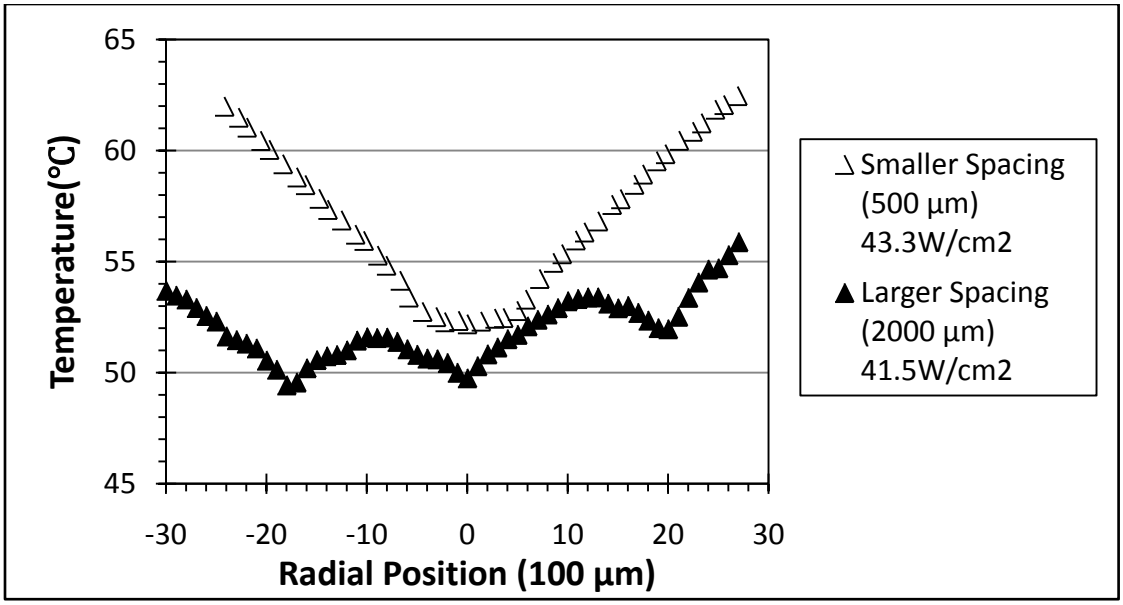

Fig. 44. Radial temperature distribution of the bare silicon surface for triple droplet stream cooling with different stream spacing (500 µm and 2000 µm) at high heat flux conditions using FC-72 at 20 °C

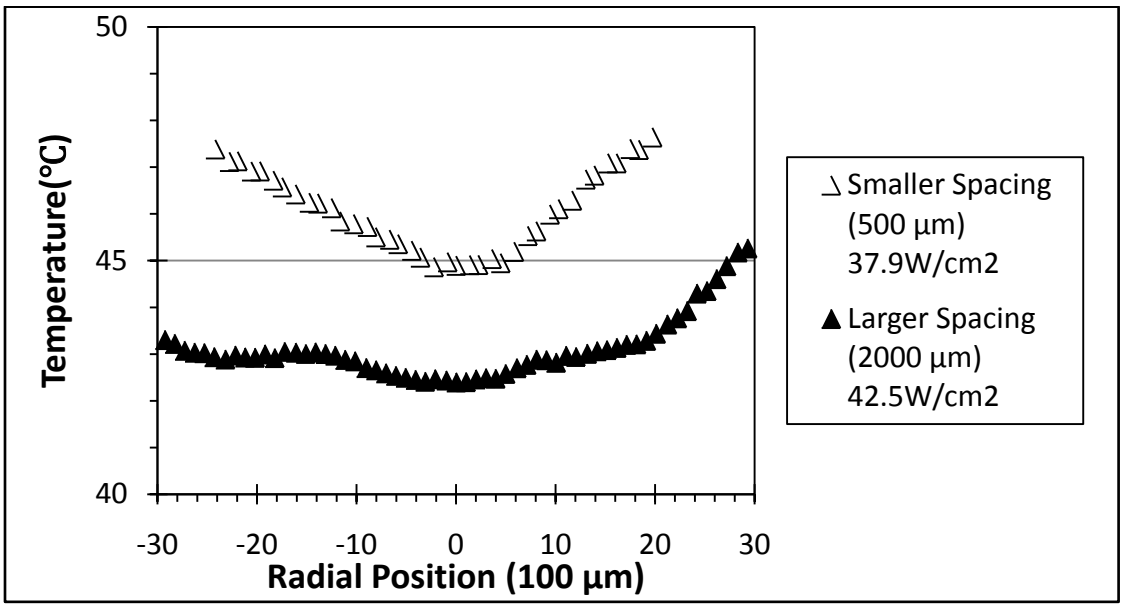

Fig. 45. Radial temperature distribution of the nano-structured surface for triple droplet stream cooling with different stream spacing (500 µm and 2000 µm) at high heat flux conditions using FC-72 at 20 °C

4.4. Increase of effective surface area

It is argued that the improved heat dissipation capability of the nano-structured surface is caused by the increased effective surface area. By using equation (7) for calculating the increased surface area where A_{add} = additional surface area, d_p = diameter of the pillar, h_p = height of the pillar, a single unit of the nano-structured surface has 6.3 % more heat transfer area.

$$A_{add} = \pi \times d_p \times h_p \quad (7)$$

A single unit on the nano-structured surface is shown in Fig. 46. When comparing single droplet results where more than 40% heat transfer was achieved, a 6.3% increase in surface area is not large enough to explain the total enhancement. Also, it cannot be used to explain different heat transfer behavior found in triple stream experiments where smaller spacing has similar behavior to the bare-silicon surface. Therefore, the author suggests that the effect of the increase in effective surface area is limited. Main heat transfer enhancement that results from the use of nano-structured surfaces can be explained by film morphology and the effective thermal diameter. Future studies elucidate the mechanism(s) responsible for enhanced heat transfer including the role of nanoscale features on film dynamics.

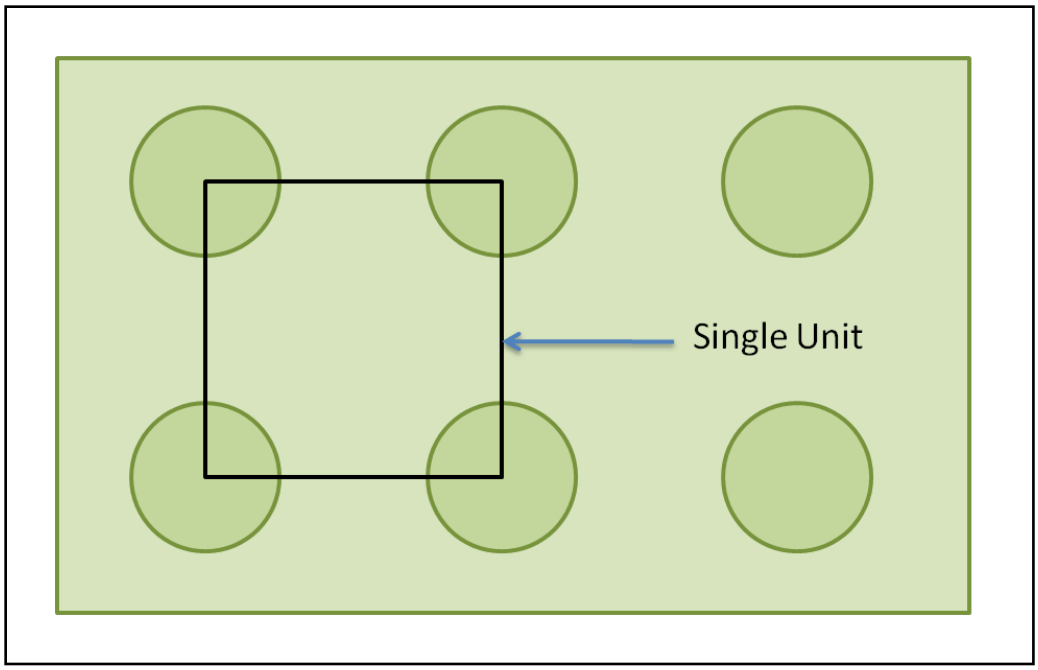

Fig. 46. Definition of nano-structure unit on the surface

4.5. Contact angle test

A contact angle test was done using a needle (N730, Hamilton Needles) to gently place a droplet on the two experimental surfaces. The outer diameter and inner diameter of the needle are 0.012 in. and 0.006 in., respectively. Images were taken using the high speed camera, and the angle was measured using Vision Assistant software. The results are shown in Fig. 47. It is observed that the static contact angle of the nano-structure surface is lower than the bare silicon surface.

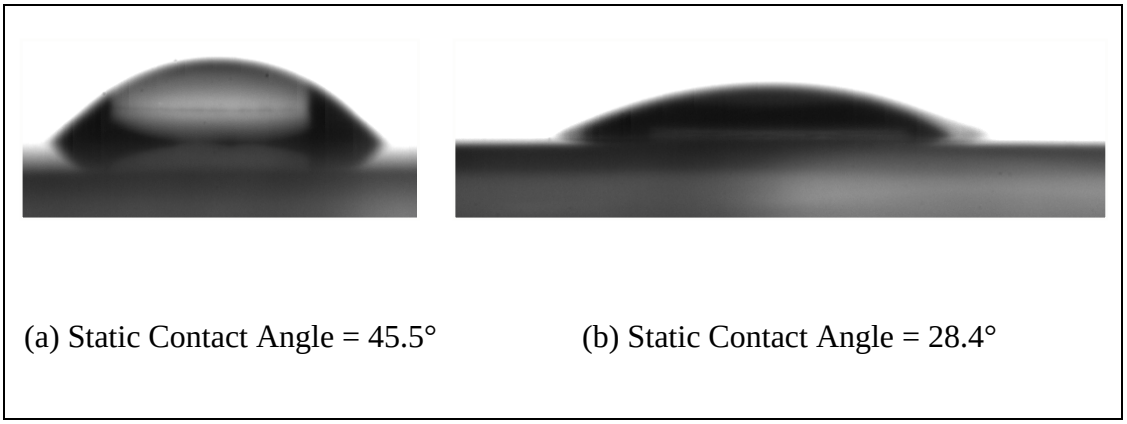

(a) Static Contact Angle = 45.5° (b) Static Contact Angle = 28.4°

Fig. 47. Static contact angle test of different surfaces using water as liquid phase and air as gas phase at 24 °C (a) bare silicon surface (b) nano-structured surface

5. CONCLUSION

Single and triple droplet impingements cooling of bare and nano-structured surfaces were performed to investigate the effect of nanoscale features on heat transfer. Two droplet stream spacing were also tested on different surfaces to understand the effect of the spacing and its influence on heat transfer. The droplet and film motion were captured using a high speed imaging system. An infrared thermal imaging technique was used to measure the surface temperature along the heat transfer area.

From the thermal image results, the author concludes that the cooling effectiveness of a nano-structured surface is far better than that of a bare silicon surface. A larger effective thermal diameter, better heat transfer curve (slope), and lower temperature gradient in the impact zone (radial distribution) were observed for the nano-structured surface in the single stream experiments, showing that the heat dissipation capability of the nano structure is better in single droplet stream experiments. The same observations were made in the triple stream experiments.

Two different stream spacing in triple droplet stream experiments show that larger spacing (2000 μm) yields better heat transfer performance by maintaining lower minimum wall temperatures and even better surface temperature distributions at high heat flux conditions. The droplet streams with smaller spacing show a wide and flat local temperature distribution, which indicate the advantage of moderating temperature gradient within a small area. With smaller stream spacing, the nano-structured surface

also shows a much better temperature distribution outside the impact zone. Effective thermal diameter data were also used to explain the different heat transfer behavior of the nano-structured surface with smaller spacing. Results indicate that the effective diameter did not change with heat fluxes when the spacing was reduced as seen in the the bare silicon heat transfer experiments.

From the high speed image results in single droplet impingement, different outer ring structures were observed on the nano-structured surface, which are evidence of the changing film dynamics caused by the nano-structured surface. With the observation that a larger outer ring structure results in better heat transfer, the author suggest that a strong heat transfer mechanism takes place in the outer ring structure. This can be indirectly confirmed by the fact that in the triple stream experiments the effective thermal diameter in the nano-structured case was independent of heat flux as in the bare silicon surface. Smaller stream spacing suppresses the crown structure and plays down the role of outer ring structure in heat transfer. Therefore, smaller stream spacing shows only slightly enhancement of minimum wall temperature in the nano-structured surface. Contact angle tests show that surface properties such as surface tension is substantially different on the nano-structured surface, which may cause different film dynamics and improved forced convection.

6. FUTURE WORKS

Future work should consider the effect of droplet frequency and phase shift between adjacent droplet impacts on heat transfer. Also, the role of nano-structure features on heat transfer through improved film dynamics (i.e. improved contact angle) or nano-scale heat transfer should be studied in greater detail. A way to elucidate the possible nano-scale heat transfer mechanisms is by conducting heat transfer tests with a surface with similar surface properties (i.e. contact angle) as the nano-structured surface to see if contact angle has more to do with improved film dynamics than the nanoscale features. The mechanism inside the outer ring structure should also be studied to understand the role of the outer ring in terms of heat transfer.

REFERENCES

[1] I. Mudawar, Assessment of high-heat-flux thermal management schemes, IEEE Transactions on Components and Packaging Technologies 24 (2001) 122-141.

[2] M. R. Pais, L. C. Chow and E. T. Mahefkey, Surface roughness and its effects on the heat transfer mechanism in spray cooling, Journal of Heat Transfer 114 (1992) 211-219.

[3] S. Toda, Study of mist cooling (1st report: investigation of mist cooling), Heat Transfer Jpn. Res. 1 (1972) 39-50.

[4] M. Monde, Critical heat flux in the saturated forced convection boiling on a heated disk with impinging droplets, Heat Transfer Jpn. Res. 8 (1979) 54-64,.

[5] I. Mudawar and T. A. Deiters, Universal approach to predicting temperature response of metallic parts to spray quenching, Int. J. Heat Mass Transfer 37 (1994) 347-362.

[6] I. Mudawar and K. A. Estes, Optimizing and predicting CHF in spray cooling of a square surface, ASME J. Heat Transfer 118 (1996) 672-679.

[7] B. Horacek, J. Kim and K. T. Kiger, Spray cooling using multiple nozzles: Visualization and wall heat transfer measurements, IEEE Transactions on Device and Materials Reliability 4 (2004) 614-625.

[8] B. Horacek, K. T. Kiger and J. Kim, Single nozzle spray cooling heat transfer mechanisms, Int. J. Heat Mass Transfer 48 (2005) 1425-1438.

[9] M. S. Sehmbey, M. R. Pais and L. C. Chow, Effect of surface material properties and surface characteristics in evaporative spray cooling, J. Thermophys. Heat Transfer 6 (1992) 505-512.

[10] E. A. Silk, J. Kim and K. Kiger, Enhanced surface spray cooling with embedded and compound extended surface structures, in: 10th Intersociety Conference on Thermal and Thermomechanical Phenomena and Emerging Technologies in Electronic Systems, 2006, P. 215-223.

[11] C. Hsieh and S. Yao, Evaporative heat transfer characteristics of a water spray on micro-structured silicon surfaces, Int. J. Heat Mass Transfer 49 (2006) 962-974.

[12] C. Sodtke and P. Stephan, Spray cooling on micro structured surfaces, Int. J. Heat Mass Transfer 50 (2007) 4089-4097.

[13] J. H. Kim, S. M. You and S. U. S. Choi, Evaporative spray cooling of plain and microporous coated surfaces, Int. J. Heat Mass Transfer 47 (2004) 3307-3315.

[14] Y. Kim, C. Choi, K. Lee and D. Han, Experimental study of spray cooling performance on micro-porous coated surfaces, Heat Mass Transfer 45 (2009) 1285-1292.

[15] S. R. Sriraman and D. Banerjee, Pool boiling studies on nano-structured surfaces, in: ASME International Mechanical Engineering Congress and Exposition, 2007, p. 317-324.

[16] M. Colburn, T. Bailey, B. J. Choi, J. G. Ekerdt, S. V. Sreenivasan and C. G. Willson, Development and advantages of step-and-flash lithography, Solid State Technology 44 (7) (2001) 67-77.

[17] S. V. Sreenivasan, C. G. Willson, N. E. Schumaker and D. J. Resnick, Low-cost nanostructure patterning using step and flash imprint lithography, Presented at Nanostructure Science, Metrology, and Technology, 2001

APPENDIX A

MEASUREMENT UNCERTAINTIES

A.1. Heat flux measurement

In the setup, there are four heat transfer components as shown in Fig. 48 including heat dissipation by the impacting droplet (Q''_{fluid}), natural convection on both sides of the heater ($Q''_{surface}$), conduction through the holder (Q''_{holder}), and conduction through the soldered electrodes ($Q''_{electrode}$). In this study, the heat loss is determined by measuring the heat that is needed to maintain the heater surface temperature with no droplet impingement taking place. The heat losses consist of the $Q''_{surface}$, Q''_{holder}, and $Q''_{electrode}$ those are driven by temperature difference between the heater and surrounding even in the absence of droplet cooling. It is assumed that the magnitude of the combined heat losses does not change appreciably when droplet cooling takes place.

The average temperature of the heater's surface and the amount of heat (heat losses) required to maintain it were recorded using the IR imaging system and data acquisition system when the entire set up reached steady state. The overall heat loss as a function of surface temperature curve is shown in Fig. 49.

Equation (8) is used for computing heat flux for spray cooling experiments:

$$Q'' = \frac{P_{in} - Q_{loss}}{A_{heater}} \quad (8)$$

The experimentally measured heat losses are in the order of 6 to 9 % of the total input power.

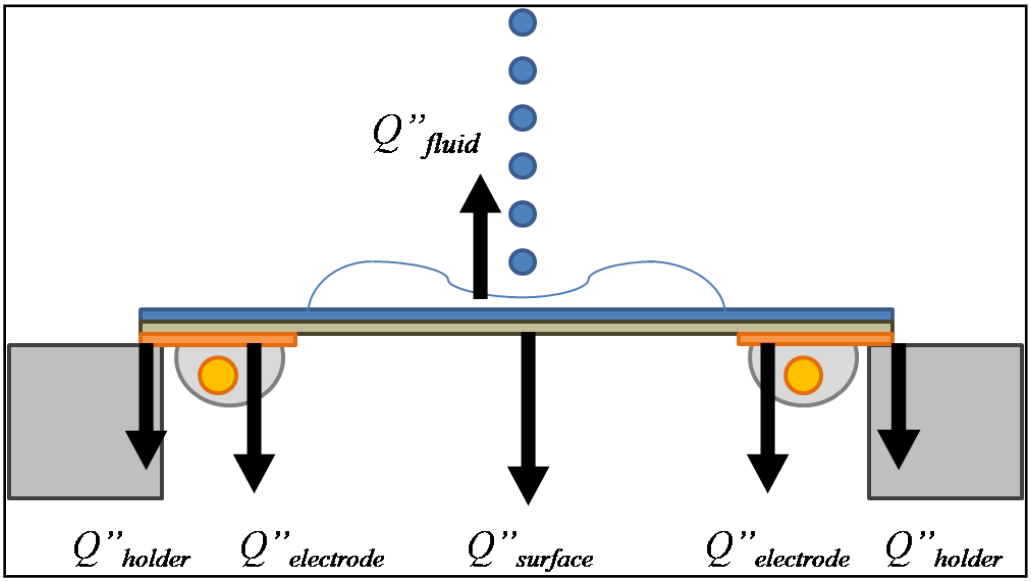

Fig. 48. Heat loss mechanisms in the heater setup

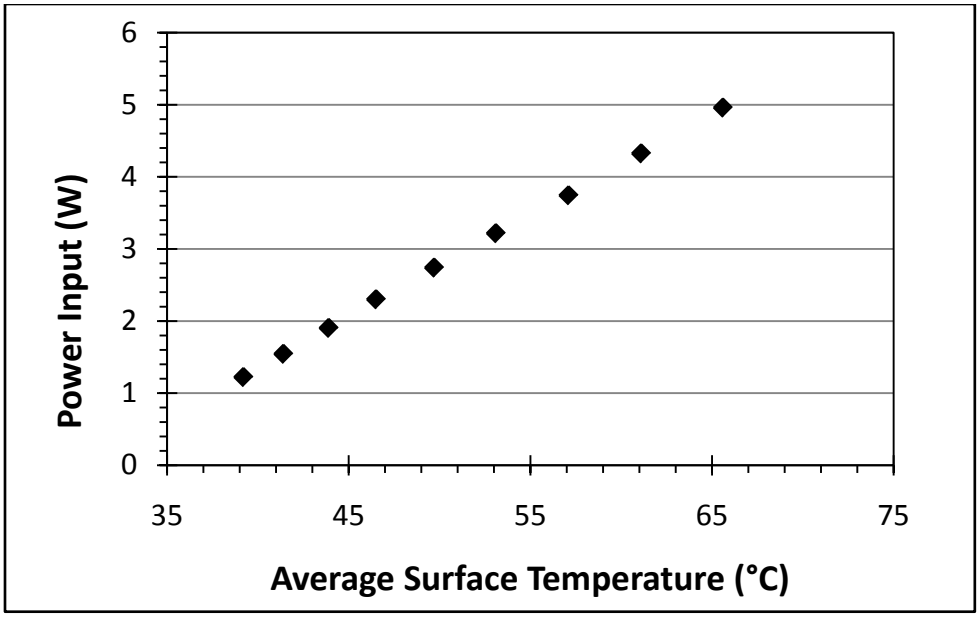

Fig. 49. Power input as a function of average surface temperature for ITO heater

A.2. Heat flux measurement uncertainty analysis

The uncertainty of heat flux calculation can be found using the Kline McClintock methodology, with the propagated error expressed as follows:

$$u_{Q"}^2 = \left(\frac{\partial Q"}{\partial V} u_V\right)^2 + \left(\frac{\partial Q"}{\partial I} u_I\right)^2 + \left(\frac{\partial Q"}{\partial T} u_T\right)^2 + \left(\frac{\partial Q"}{\partial A} u_A\right)^2 \quad (9)$$

Where $u_{Q"}$ = uncertainty of the heat flux, u_V = uncertainty of the voltage reading, u_I = uncertainty of the current reading, u_T = uncertainty of the temperature reading, u_A = uncertainty of the heater surface area.

The errors associated with the measurement of voltage and current of power supply GEN- 600-2.7 used in this study according to manufacturers were:

$$u_V = 0.1\ \%\ \text{reading} + 0.2\%\ \text{rated output voltage}$$

$$u_I = 0.1\ \%\ \text{reading} + 0.4\%\ \text{rated output current}$$

The heat flux uncertainty was found to be 1.24 W/cm^2. This is approximately 7% of the maximum heat flux obtained during the single droplet cooling impingement experiment.

A.3. Crown diameter measurement uncertainty

The Vision Assistant software (National Instruments) was used to measure the inner and outer crown diameter of the impact zone produced by droplet impingement. In the crown diameter measurement, a magnification of 5.88 μm/pixel was used. An estimated uncertainty of ±4 pixels was considered for crown diameter measurements in this study. Therefore, the corresponding uncertainty for inner and outer crown diameter measurement was estimated to be ±24 μm.

A.4. Droplet diameter measurement uncertainty

The Image Analysis Tool from National Instruments was used to measure the projected vertical surface area of each droplet which in turn was used to compute droplet diameter. A scale of 1.5 μm/pixel was used for these measurements. The droplet diameter uncertainty was found to be ±7.5 μm.

A.5. Droplet velocity measurement uncertainty

The velocity of the droplet was calculated from equation (10), where L = the distance between droplets, and f = the input frequency of the function generator.

$$v_d = L \times f \quad (10)$$

Uncertainty on velocity measurements was then found using equation (11),

$$u_{v_d}^2 = \left(\frac{\partial v_d}{\partial L} u_L\right)^2 + \left(\frac{\partial v_d}{\partial f} u_f\right)^2 \quad (11)$$

The distance of each droplet was measured using a magnification of 4.5 μm/pixel. With an uncertainty of ±4 pixels, the corresponding uncertainty was found to be ± 20 μm. Frequency uncertainty of signal generator (BK Precision Model 4011A) used in this study is ±10 Hz. When substitute into equation (11), an uncertainty of 0.14 m/s is obtained for velocity measurements

A.6. Temperature measurement of the IR camera using an ITO heater

The temperature of an object in infrared thermography is obtained by measuring irradiance W (W/str-m^2). In this study, the temperature was measured at the ITO heater surface. The irradiance components received by the IR camera in the heater setup are shown in Fig. 50.

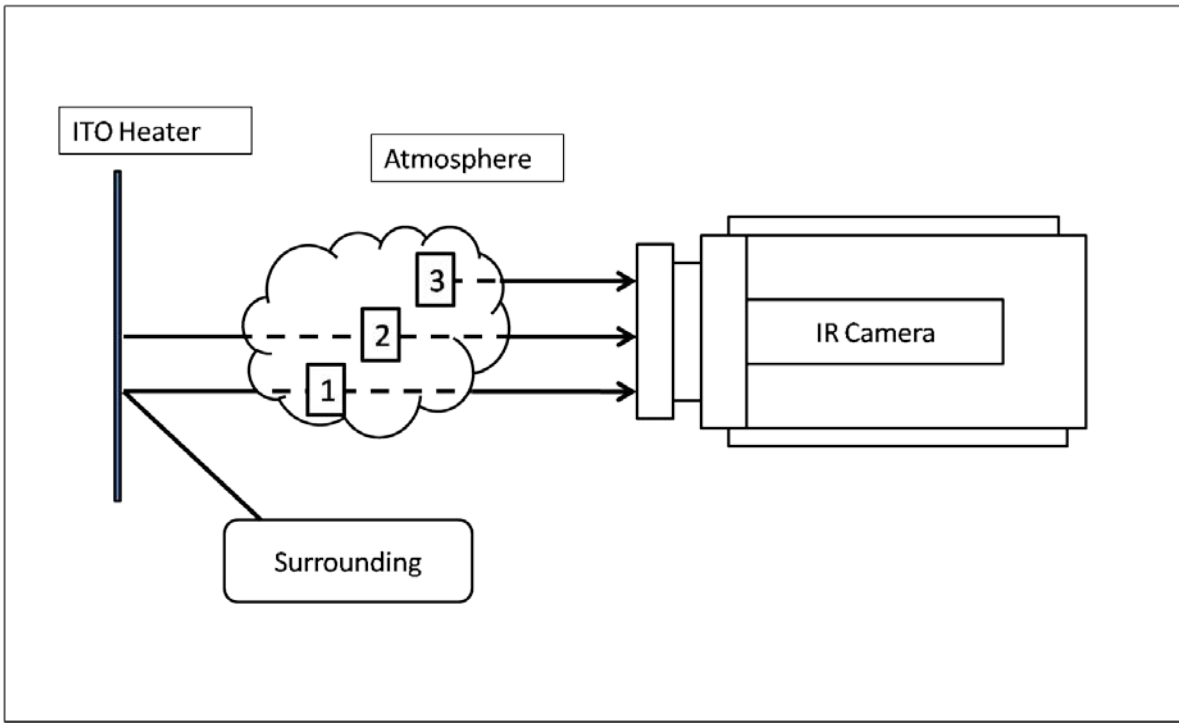

Fig. 50. Schematic diagram of infrared temperature measurement technique

The three main irradiance components come from (1) irradiance from the surroundings reflected on ITO surface, and transmitted through ambient air, (2) irradiance emitted from ITO surface, and transmitted through ambient air, and (3) irradiance emitted by ambient air.

These three components can be expressed individually in the following equation for total irradiance:

$$W_{tot} = \rho_{ITO} \times \tau_{atm} \times W_{surr} + \varepsilon_{ITO} \times \tau_{atm} \times W_{ITO} + \varepsilon_{atm} \times W_{atm} \quad (12)$$

Where ρ = reflectivity, τ = transmissivity, ε = emissivity. In order to simplify equation (12), the following assumptions are made:

1. At any surface, all the energy is absorbed, reflected or transmitted. This can be expressed as equation

   $$\alpha + \rho + \tau = 1 \quad (13)$$

2. ITO heater surface is a graybody, so that the emissivity and absorptivity of the ITO are the same and constant in the wavelength of interest. This assumption is valid for small temperature ranges. The following equation is used to take into account the assumption.

   $$\alpha_{ITO} = \varepsilon_{ITO} \quad (14)$$

3. The ITO surface is opaque, so that the transmissivity in the wavelength of interest is zero. (Equation (15)).

   $$\tau_{ITO} = 0 \quad (15)$$

4. Ambient air is considered to be a graybody and the reflectivity is assumed to be zero. The following equations are obtained.

$$\alpha_{atm} = \varepsilon_{atm} \quad (16)$$

$$\rho_{atm} = 0 \quad (17)$$

From these assumptions, equation (12) can be simplified by taking into account equations (13)-(17). Equation (12) then becomes:

$$W_{tot} = (1 - \varepsilon_{ITO}) \times \tau_{atm} \times W_{surr} + \varepsilon_{ITO} \times \tau_{atm} \times W_{ITO} + (1 - \tau_{atm}) \times W_{atm} \quad (18)$$

The sensor of the IR camera receives radiation energy according to equation (18). The irradiance received by the sensor is then converted to an output signal (volts). This output signal is received, amplified, and converted into a digital value D (units = digital counts) by the detector. The digital readings of the camera (D) and the irradiance (W) are related as per the following equation:

$$D = A + B \times W \quad (19)$$

Where A = constant associated with the internal irradiance effects of IR camera, and B = constant associated with the detector response to irradiance.

Constant A is a fixed response constant of the sensor due mostly to the heat generation of the electronic components inside the camera. Constant B represents the linear response of the camera to incoming irradiance.

In order to obtain an expression of absolute temperature from digital readings, an approximation of the absolute blackbody temperature as a function of irradiance is used.

$$T = F + G \times \ln(W) \quad (20)$$

Where F and G are constants used to represent the Planck Function. Irradiance and absolute temperature of a blackbody are related through the Planck function in which the irradiance varies exponentially with temperature.

When substituting equation (19) into (20), the following equation is obtained:

$$T = A^* + B^* \ln(D) \quad (21)$$

Where A^* = constant associated with the internal effects of an IR camera, and B^* = constant associated with the detector response of an IR camera. By measuring the IR camera response to a blackbody at different temperatures, the determination of constants A^* and B^* is obtained using the least square fit technique on the temperature curve. The calibration was performed by the IR camera manufacturer (FLIR system) using NIST-traceable calibrated blackbody sources and thermocouples.

The only unknown in equation (21) is D. When combining equation (18) and (19), the equivalent digital reading of the ITO heater (D_{ITO}) can be obtained as follows:

$$D_{ITO} = \frac{1}{\varepsilon \times \tau} D_{tot} - \frac{1-\varepsilon}{\varepsilon \times \tau} D_{surr} - \frac{1-\tau}{\varepsilon \times \tau} D_{atm} \quad (22)$$

Where ε = emissivity of the ITO heater, and τ = transmissivity of the atmosphere. By using equation (21) to express D_{surr} and D_{atm} and substituting these equations with equation (22) into equation (21), the following equation is obtained.

$$T_{obj} = A^* + B^* \times ln\left(\frac{1}{\varepsilon \times \tau} D_{tot} - \frac{1-\varepsilon}{\varepsilon \times \tau} e^{\left(\frac{T_{surr} - A^*}{B^*}\right)} - \frac{1-\tau}{\varepsilon \times \tau} e^{\left(\frac{T_{atm} - A^*}{B^*}\right)}\right) \quad (23)$$

The digital value of the object is then used in equation (23) to obtain the temperature of the object.

This equation is embedded in the Examin IR software (FLIR system) used to interact with the IR camera. Examin IR requires surrounding and ambient air temperatures, emissivity of the ITO heater, and transmissivity of ambient air to be able to provide surface temperature. The software has an embedded algorithm for calculating transmissivity of ambient air using relative humidity of air, temperature, and distance from object to the camera. This information is measured and recorded in a datasheet prior to each test in this study. At small distances and laboratory conditions, transmissivity is considered to be one.

A.7. Emissivity measurement

In this study, standard ASTM E1933 “Standard test methods for measuring and compensating for emissivity using infrared imaging radiometers” was used to measure the emissivity of the ITO heater surface. In ASTM E1933, the emissivity is measured using a reference material of known emissivity. The reference material used in this study was an electrical vinyl tape Super 88 with a known emissivity value of $\varepsilon = 0.95 \pm 0.05$.

The first step is to measure the digital reading of the irradiance from surroundings where the temperature measurement will be performed. This is done by placing a reflective foil over the surface to be measured before recording digital counts. The reflective foil would suppress the irradiation from the object reaching the camera allowing only reflection from the surroundings to reach the camera. Due to the small distance between the camera and the object, the effect of ambient air is negligible.

In the next stage, a coating of known emissivity is applied on a small section of the surface of the ITO heater. The ITO heater is then heated to at least 30 °C above the temperature of the surroundings. This is done by placing the ITO heater into a laboratory oven for 3 hours at three different temperatures.

The number of irradiance counts of both the target and object with known emissivity are both measured and recorded. The emissivity is then calculated using the following equation,

$$\varepsilon_{ITO} = \frac{D_{tot} - D_{surr}}{D_{ref} - D_{surr}} \varepsilon_{ref} \quad (24)$$

Where D = digital reading of the camera in number of counts. Subscript ref refers to the total digital value of the reference object. The calculated emissivity value at different temperatures is presented in Table 10.

Table 10
Emissivity values of ITO surface at different temperatures

Temperature (°C)	Emissivity
33.3	0.79
49.2	0.798
56	0.786

The equation for error propagation in emissivity measurement is as follows:

$$\frac{\Delta\varepsilon_{\mathrm{ITO}}}{\varepsilon_{\mathrm{ITO}}} = \sqrt{\left(\frac{\Delta\varepsilon_{ref}}{\varepsilon_{ref}}\right)^2 + 2\Delta D^2\left(\frac{1}{(D_{tot} - D_{surr})^2} + \frac{1}{(D_{ref} - D_{surr})^2}\right)} \tag{25}$$

The uncertainty value of the counts readings was found by computing the standard deviation (σ) of statistically significant readings of the uniform target. Assuming a normal distribution of the measurements, a range of three-standard deviations (3σ) gives a probability of 99.7% that the result can be explained within the range. Applying equation (25), the emissivity uncertainty of the equivalent surface was found to be 0.792 ± 0.043.

A.8. Temperature measurement uncertainty

The first step to compute the temperature uncertainty of the camera is to plot the apparent temperature (Fig. 51) and the counts digital readings of the camera over a temperature range of interest. Apparent temperature is the temperature of the object when emissivity is set to one.

Using the least squares method and equation (21), the values of the calibration constants of the camera (A^* and B^*) were found be $A^* = -1014.8$ and $B^*=104.97$.

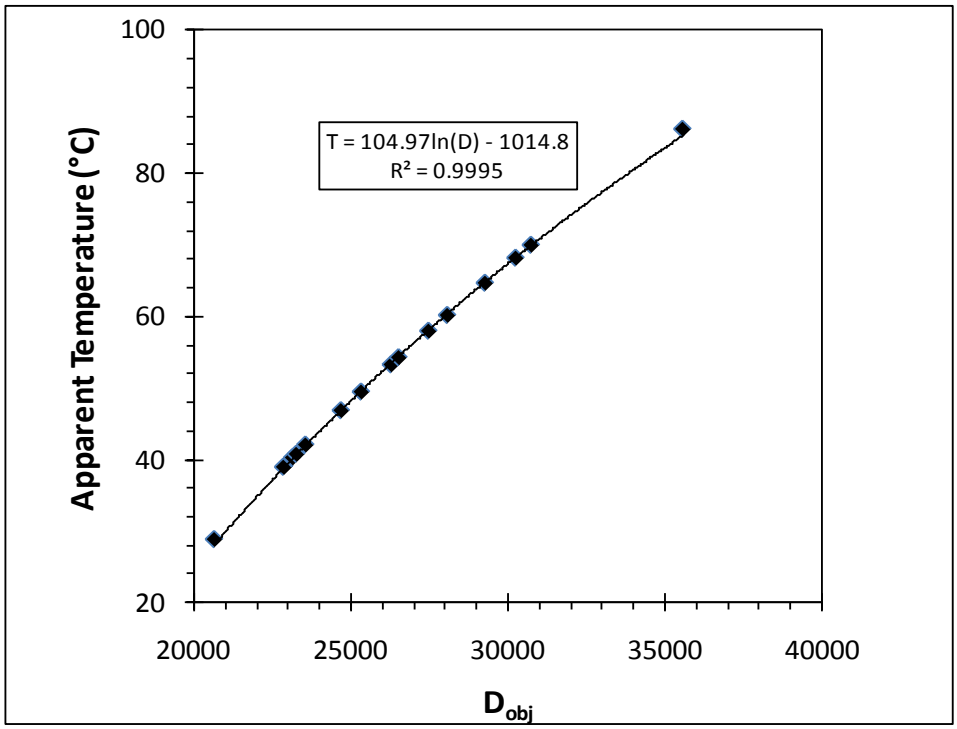

Fig. 51. Apparent surface temperature as a function of digital counts using curve fit

Using equation (18) and the Kline McClintock methodology, the temperature uncertainty can be found as follows:

$$\Delta T = \frac{B^* \times \Delta D_{ITO}}{D_{ITO}} \qquad (26)$$

At small distances between the camera and target, the effects of water vapor in ambient air are considered to be negligible. In those cases, it is safe to assume that τ_{atm}= 1 and ρ_{atm}= 0. Equation (26) is then written as,

$$\Delta T = \frac{B^*}{D_{tot} - (1-\varepsilon_{ITO})D_{surr}} \left[\Delta D_{tot}^2 + \Delta D_{surr}^2 \left(1 - \varepsilon_{eq}\right)^2 + \Delta \varepsilon_{ITO}^2 \left(\frac{-D_{ITO} + D_{surr}}{\varepsilon_{ITO}} \right)^2 \right]^{1/2} \qquad (27)$$

Where D_{tot} is obtained by taking readings of the object in digital counts mode, and D_{surr} is obtained by taking readings at the target location covered with a reflective foil as indicated previously. The uncertainty values of the digital reading are obtained by computing the standard deviation of statistically significant samples of the total and surroundings.

After applying equation (27) for three different digital reading values of the equivalent surface, the temperature reading with its uncertainty were computed and are listed in Table 11.

Table 11
Temperature uncertainty at different temperature values

Temperature (°C)	Temperature Uncertainty (°C)
30	0.5
40	0.8
55	1.6

The variation of uncertainty is due to an increment of the difference of $D_{tot} - D_{surr}$ as represented by the third term in equation (27). If emissivity had a deterministic value, the surface temperature uncertainty would become ± 0.06 °C at an apparent temperature of 55 °C.

VITA

Yen-Po Lin received his Bachelor of Science degree in the Mechanical Engineering from National Tsing Hua University in Taiwan in 2006.

He became a master's student in 2008 in the Department of Mechanical Engineering at Texas A&M University, College Station. Yen-Po joined the Spray Cooling Laboratory as a graduate research assistant with Dr. Jorge L. Alvarado as his research advisor in Spring 2009.

His research was about the single and multiple droplet impingement cooling on nano-structured surfaces, under the guidance of Dr. Jorge L. Alvarado, co-chair of committee member Dr. Debjyoti Banerjee, and committee member Dr. Yassin A. Hassan. In his work, he was able to characterize important parameters in the droplet cooling system. He received his Master of Science degree in August 2010.

Email Address: yplin113@gmail.com

Physical Address: Department of Mechanical Engineering
c/o Dr. Alvarado or Dr. Banerjee
Texas A&M University
College Station, TX 77843-3123

Research Interests: Electronics Cooling, Thermal Management, Nano-fabrication Multiphase Flow and Heat Transfer, Multi-scale Energy Transport